COGNITIVE NEUROSCIENCE

Uncovering a tripartite landmark in posterior cingulate cortex

Ethan H. Willbrand[1,2]†, Benjamin J. Parker[2]†, Willa I. Voorhies[1,2], Jacob A. Miller[2], Ilwoo Lyu[3], Tyler Hallock[1], Lyndsey Aponik-Gremillion[4], Seth R. Koslov[5], Alzheimer's Disease Neuroimaging Initiative‡, Silvia A. Bunge[1,2], Brett L. Foster[5], Kevin S. Weiner[1,2]*

Understanding brain structure-function relationships, and their development and evolution, is central to neuroscience research. Here, we show that morphological differences in posterior cingulate cortex (PCC), a hub of functional brain networks, predict individual differences in macroanatomical, microstructural, and functional features of PCC. Manually labeling 4511 sulci in 572 hemispheres, we found a shallow cortical indentation (termed the inframarginal sulcus; *ifrms*) within PCC that is absent from neuroanatomical atlases yet colocalized with a focal, functional region of the lateral frontoparietal network implicated in cognitive control. This structural-functional coupling generalized to meta-analyses consisting of hundreds of studies and thousands of participants. Additional morphological analyses showed that unique properties of the *ifrms* differ across the life span and between hominoid species. These findings support a classic theory that shallow, tertiary sulci serve as landmarks in association cortices. They also beg the question: How many other cortical indentations have we missed?

INTRODUCTION

Elucidating the relationship between structural and functional features of the cerebral cortex and explaining how individual differences in brain structure-function correspondences develop across the life span and evolve across species are central endeavors in neuroscience research (*1*–*4*). Of the many structural features to consider, the indentations of the human cerebral cortex (HCC), or sulci, are particularly interesting because a majority (60 to 70%) of the HCC is buried within sulci (*5*, *6*). Concomitantly, classic and modern studies test whether sulci can be used as landmarks that help navigate the complicated relationship among microstructural, macrostructural, functional, and network features of the human brain (*7*–*13*). For example, two types of sulci (*7*, *8*) are considered particularly useful: limiting sulci, which identify a transition between areas or cortical maps [e.g., the mid-fusiform sulcus (*mfs*) and four different cytoarchitectonic areas (*11*, *13*)] or axial sulci, which colocalize (or are always located within) a cortical area [e.g., the calcarine sulcus and primary visual cortex (V1) (*9*, *10*)]. In addition to the fact that the former is a useful landmark identifying transitions between cortical areas or maps, while the latter is a useful landmark identifying a cortical area, sulci themselves are also used as corridors or entry points in neurosurgery (*14*). Thus, precise understanding of a sulcal landscape in a given cortical expanse not only provides structural-functional understanding but also provides translational applications.

With these goals in mind, although most structural-functional studies historically focused on prominent folds (termed primary sulci) in primary sensory cortices, growing evidence shows that individual differences in the morphology of shallow indentations in the cerebral cortex, known as tertiary sulci, co-occur with individual differences in the functional organization of association cortices, as well as individual differences in cognition with translational applications (*13*, *15*–*22*). While these findings build on a classic theory (*23*) suggesting that tertiary sulci are behaviorally meaningful landmarks supporting the functional layout of cognitive representations in association cortices, tertiary sulci have yet to be explored in key association cortices such as posteromedial cortex (PMC).

PMC is routinely considered a central hub of the default mode network (DMN) (*24*–*27*) and implicated in a broad array of cognitive functions, such as episodic memory, self-referential processing, spatial navigation, and cognitive control (*24*, *25*, *28*–*33*). PMC also has unique anatomical (*29*, *34*), metabolic (*24*), functional (*35*), developmental, and evolutionary properties (*30*, *36*, *37*). Despite this progress in identifying different functions and properties of PMC, the functional neuroanatomy of human PMC remains poorly understood. Precise understanding of its functional-anatomic subdivisions has been impeded by a lack of consensus regarding its basic anatomy. For example, many different anatomical labels and demarcations are used to refer to the same macroanatomical subdivisions within PMC (Fig. 1). Furthermore, previous studies often did not consider sulcal patterning within individual participants (*25*–*27*, *38*), especially the patterning of shallow tertiary sulci (Materials and Methods), which are often overlooked and excluded in neuroimaging software packages for a variety of methodological reasons as discussed previously (*21*, *22*, *39*).

In the present study, we implemented a multimethod approach to explore the functional and microstructural relevance of shallow, putative tertiary sulci in PMC. To do so, we manually defined sulci at the individual-participant level in discovery ($N = 36$) and replication ($N = 36$) young adult samples using the most recent definitions of PMC sulci (Materials and Methods) (*40*). Through this process, we found a new putative tertiary sulcus (which we refer to as the

[1]Department of Psychology, University of California, Berkeley, Berkeley, CA 94720 USA. [2]Helen Wills Neuroscience Institute, University of California, Berkeley, Berkeley, CA 94720 USA. [3]Department of Computer Science and Engineering, Ulsan National Institute of Science and Technology, Ulsan 44919, South Korea. [4]Baylor College of Medicine, Houston, TX 77030, USA. [5]Department of Neurosurgery, Perelman School of Medicine, University of Pennsylvania, Philadelphia, PA 19104, USA.
*Corresponding author. Email: kweiner@berkeley.edu
†These authors contributed equally to this work as co–first authors.
‡Data used in preparation of this article were obtained from the Alzheimer's Disease Neuroimaging Initiative (ADNI) database (adni.loni.usc.edu). As such, the investigators within the ADNI contributed to the design and implementation of ADNI and/or provided data but did not participate in analysis or writing of this report. A complete listing of ADNI investigators can be found at: https://adni.loni.usc.edu/wp-content/uploads/how_to_apply/ADNI_Acknowledgement_List.pdf

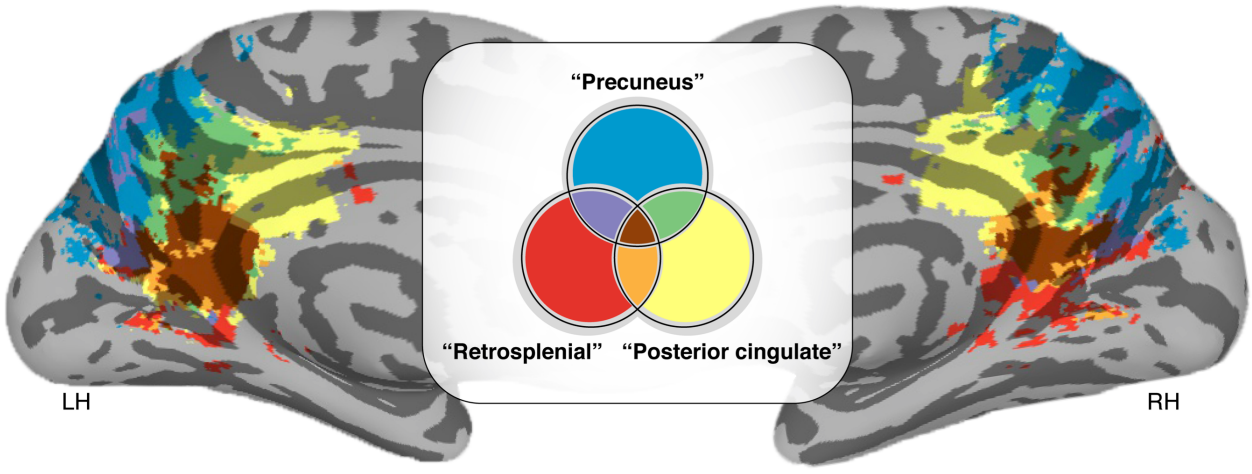

Fig. 1. Different names for the same cortical expanse within PMC. MNI152 inflated cortical surface showing Neurosynth (https://neurosynth.org) (*44*) association maps based on the following neuroanatomical search terms: "Posterior cingulate," "Precuneus," and "Retrosplenial" in the left hemisphere (LH) and right hemisphere (RH). Colors indicate the location and areas of overlap across the reference studies (947, 1014, and 131 studies, respectively) resulting from each search term. As depicted here, different anatomical labels are used to refer to the same macroanatomical subdivisions of PMC in which 66.3% of the voxels in PMC across these studies have multiple names.

inframarginal sulcus, *ifrms*) within posterior cingulate cortex (PCC), a subregion of PMC, that is absent from neuroanatomical atlases (Supplementary Materials; fig. S1). In light of this discovery, our subsequent analyses focused on quantifying the structure and function of the *ifrms*. Using structural magnetic resonance imaging (MRI) and cortical surface reconstructions, we first characterized the incidence rates and anatomical features (sulcal depth, cortical thickness, and myelination) of the *ifrms* in young adults, relative to neighboring sulci. These analyses indicate that the *ifrms* is a landmark identifying a cortically thick and lightly myelinated locus within PCC. Second, we quantified the relationship between data-driven definitions of functional regions (*41*) and PMC sulcal definitions in young adults showing that the *ifrms* predicts the location of PCC regions within the cognitive control network (CCN). We further showed that this structural-functional coupling generalized to additional parcellations in individual participants (*42*), as well as group (*43*) and meta-analyses [i.e., Neurosynth (*44*) and recent work by the Organization for Human Brain Mapping Workgroup for Harmonized Taxonomy of Networks (OHBM WHATNET) (*45*)] consisting of hundreds of studies and thousands of participants. Third, we quantified developmental and evolutionary differences in the morphology of the *ifrms* by performing cross-sectional comparisons across three age groups (juveniles, young adults, and elderly adults) for two hominoid species (humans and chimpanzees). After manually defining more than 4000 sulci in 572 hemispheres, these analyses showed that while the *ifrms* is identifiable in all human hemispheres examined, it is only identifiable in a subset of chimpanzee hemispheres. Moreover, we observed differences in cortical thickness and depth between age groups and species. Fourth, we assessed the accuracy with which the *ifrms* could be automatically defined, using novel deep learning algorithms. These algorithms showed that the *ifrms* is more predictable than other PMC sulci that are more prominent in terms of depth and surface area. As we share these algorithms with the field, these tools should help expedite and guide the labeling of PMC sulci in future studies in neurotypical (NT) individuals and different patient populations. Together, we identify a new landmark within PCC, providing important progress in elucidating this unique region's functional organization and further supporting the significance of tertiary sulci in functional brain organization.

RESULTS

The *ifrms*: A new shallow indentation in PCC

We first manually defined both deep and shallow sulcal indentations in the PCC and precuneal cortex (PRC) within PMC in discovery (N = 36) and replication (N = 36) samples of young adults (22 to 36 years old) from the Human Connectome Project (HCP). A total of 8 to 11 PMC sulci were identifiable within each hemisphere (Fig. 2; tables S1 and S2; and figs. S2, S4, and S5). Through this process, we found a new putative tertiary sulcus that, through an exhaustive review of historical and modern neuroanatomical atlases (Supplementary Materials; fig. S1), has yet to be named. Specifically, while previous studies qualitatively documented one or many indentations in the PCC, to our knowledge, no study has quantitatively defined these indentations beyond qualitative variable descriptions, such as vertical extensions of the callosal or cingulate sulci or as dimples in PCC (see the Supplementary Materials and fig. S1 for historical analyses).

As this shallow indentation is always located underneath the marginal ramus of the cingulate sulcus (*mcgs*) in every hemisphere, we named this sulcus the *ifrms*. While our subsequent analyses focused on the structure and function of the *ifrms*, our sulcal definitions in individual participants also identified consistent and variable features of the sulcal patterning within PCC and PRC. In terms of consistency, in PRC, we highlight that while recent studies acknowledge a precuneal sulcus (*prcus*) (*30*, *40*, *46*), we identified separate posterior (*prcus-p*), intermediate (*prcus-i*), and anterior (*prcus-a*) precuneal sulci in every hemisphere in both datasets (tables S1 and S2 and figs. S2, S4, and S5). In terms of variability, in PCC, we also identified shallow sulci either underneath the splenial sulcus (*spls*), which we refer to as the sub-*spls* (*sspls*), or just anterior to the *ifrms* in a subset of hemispheres (tables S1 and S2 for incidence rates). While the latter sulcus was recently identified as the intracingulate sulcus (*47*), from our measurements, there are as many as seven shallow sulci along the length of the cingulate gyrus. Thus, we refer to this

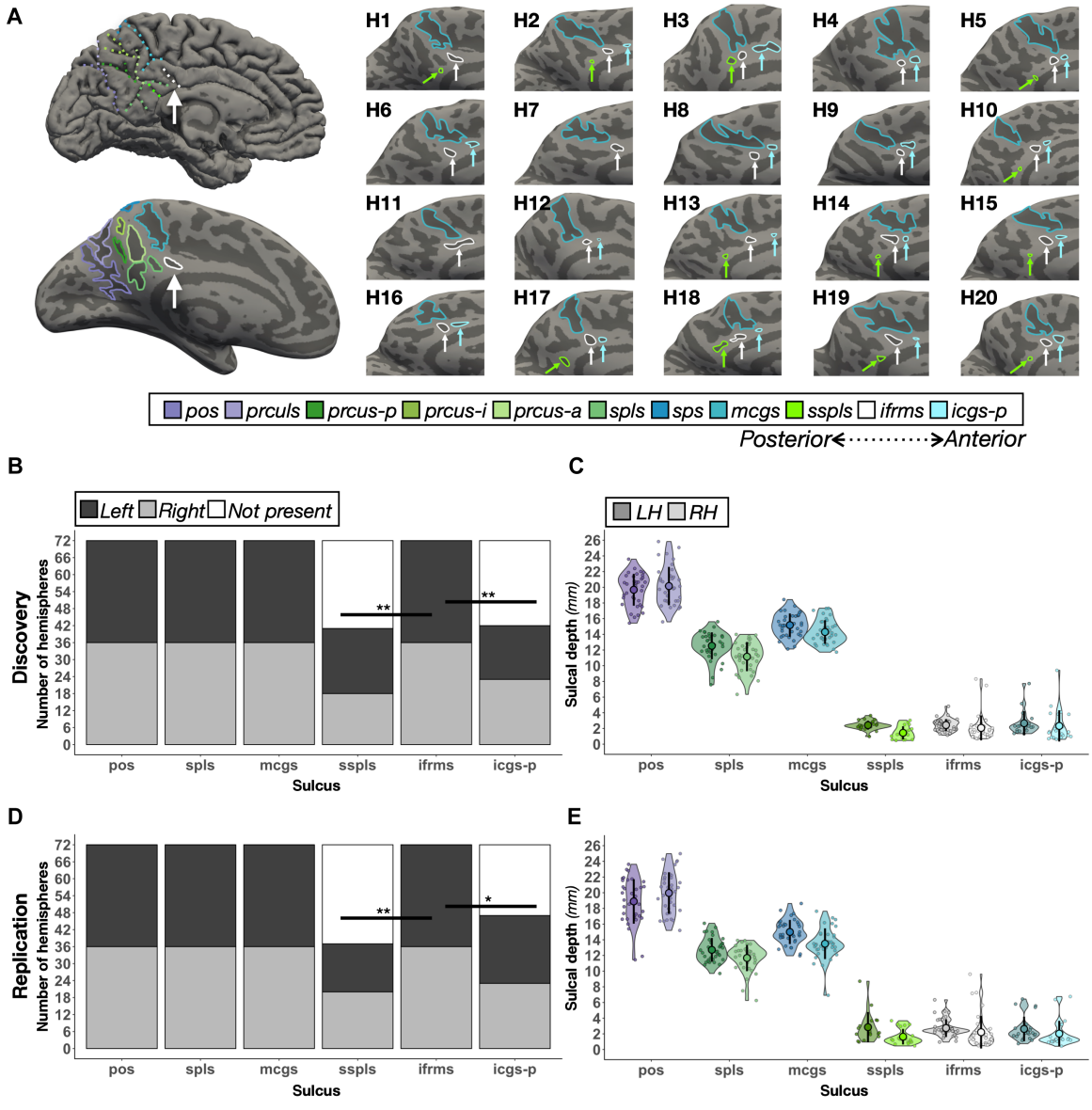

Fig. 2. The *ifrms*, but not other shallow sulci in PMC, are identifiable in every hemisphere. (**A**) Top left: A cortical surface reconstruction of an individual LH. Sulci, dark gray; Gyri, light gray. Individual sulci are depicted by dotted colored lines (legend). Bottom left: The same cortical surface but inflated. Right: Twenty example hemispheres from the discovery sample. Each hemisphere is indicated by H1, H2, etc. RH images are mirrored so that all images have the same orientation. Each shallow sulcus is designated with an arrow to highlight the consistent location of the *ifrms* underneath the *mcgs*. (**B**) Stacked bar plots illustrate the incidence rates of the three shallow sulci (*ifrms*, *sspls*, and *icgs-p*) relative to three deep sulci (*pos*, *spls*, and *mcgs*) in the discovery sample ($N = 72$ hemispheres; dark gray, LH; light gray, RH; white, absent). The *ifrms* is present in every hemisphere, while the *sspls* and *icgs-p* are not (table S1; $^*P < 0.05$, $^{**}P < 0.01$). (**C**) Sulcal depth (in millimeters) for each individual participant (small colored circles) in the discovery sample. The mean (large colored circles), SD (black line), and kernel density estimate (colored violin) are plotted for each sulcus (LH, darker shades; RH, lighter shades) (**D**) The same as (B) but for the replication sample ($N = 72$ hemispheres). As in (B), the *ifrms* is present in every hemisphere, while the *sspls* and *icgs-p* are not (Table S2). (**E**) The same as (C) but for the replication sample.

sulcus as the posterior intracingulate sulcus (*icgs-p*), which, when present, is located underneath the body of the *cgs*, while the *ifrms* is identified more posteriorly underneath the *mcgs*. Unlike the *ifrms*, the incidence rates of *icgs-p* and *sspls* varied substantially by hemisphere (discovery: $\chi^2 = 42.54$, df = 2, $P < 0.001$; replication: $\chi^2 = 45$, df = 2, $P < 0.001$; Fig. 2, B and D, and tables S1 and S2).

As shallowness relative to other sulci is a defining morphological feature of tertiary sulci (*11*, *13*, *22*), we tested whether these novel sulci (*sspls*, *ifrms*, and *icgs-p*) were significantly more shallow than surrounding sulci. Across hemispheres and datasets, the *sspls*, *ifrms*, and *icgs-p* were shallower than other PMC sulci (P values < 0.001, Tukey's adjustment; Fig. 2, C and E, and fig. S2). Beyond descriptive labeling, we also quantified the intersections between the novel shallow sulci (*ifrms*, *sspls*, and *icgs-p*) relative to other PMC sulci. Specifically, in the neuroanatomical literature, it is common to qualitatively describe sulcal "types" on the basis of fractionation and intersection with surrounding sulci [for two such recent examples, see (*11*, *48*)]. While useful for describing the sulcal relationships in a given cortical expanse,

this classic approach is qualitative in nature. Therefore, in line with recent work (*22*), we implemented a quantitative approach to relate the sulcal intersections between hemispheres within and across datasets (Materials and Methods; fig. S3 and tables S3 to S6). This quantitative approach revealed a high positive correlation between hemispheres within each sample (discovery: $r = 0.74$ and $P < 0.001$; replication: $r = 0.9$ and $P < 0.001$; fig. S3) and between samples [right hemisphere (RH): $r = 0.94$ and $P < 0.001$; left hemisphere (LH): $r = 0.82$ and $P < 0.001$).

To ensure that the computational processes used to generate the cortical surface reconstruction from individual participant MRI data did not artificially create shallow sulci, we also sought to identify shallow PMC sulci within individual postmortem brains (Fig. 3) (*49*). In 22 labeled postmortem hemispheres, the *ifrms* was again identifiable in each hemisphere, while the *sspls* and *icgs-p* were not. The *sspls* was present in 90.91% of LH and RH (20 of 22), and the *icgs-p* was found in 63.64% of LH and RH (14 of 22).

The *ifrms* identifies a cortically thick and lightly myelinated cluster in PCC

Regions positioned earlier in cortical processing hierarchies are typically cortically thin and heavily myelinated (for example, V1) (*37*). Conversely, regions positioned later in the hierarchy are typically cortically thick and lightly myelinated (for example, face-selective regions on the fusiform gyrus) (*50*, *51*). Thus, the ratio between cortical thickness and myelination is a metric related to the positioning of a region in a cortical processing hierarchy. Recent work identified a focal cluster within PCC that is cortically thick and lightly myelinated (*33*, *43*) but did not consider covariation with sulcal morphology. As this previously identified cluster was positioned directly under the *mcgs*—in the vicinity of the sulcus we have termed the *ifrms*—we tested the targeted hypothesis that the *ifrms* is cortically thicker and more lightly myelinated than other PMC sulci. To do so, we first extracted cortical thickness and myelination T1-weighted/T2-weighted (T1w/T2w ratio) (*43*) values from each sulcal label (Materials and Methods). We then calculated the ratio between cortical thickness and myelination. Across both samples and hemispheres, the *ifrms* had the greatest thickness/myelination ratio within PCC (Fig. 4B). Impressively, when viewing the thickness/myelination map on the cortical surface, the *ifrms* colocalized with this focal anatomical ratio of macroanatomical and microstructural features in PCC (Fig. 4A; see figs. S6 and S7 for the thickness/myelination profiles of all 11 PMC sulci, as well as the individual thickness and myelination values of the four PMC sulci analyzed here).

In each participant, the *ifrms* and *sspls* appeared, qualitatively, to be cortically thicker and more lightly myelinated than the deeper sulci positioned above them (*mcgs* and *spls*, respectively). To directly quantify this effect, we conducted three-way analyses of variance (ANOVAs) with factors sulcal type (deep and shallow), PMC position [anterior (*mcgs* and *ifrms*) and posterior (*spls* and *sspls*)], and

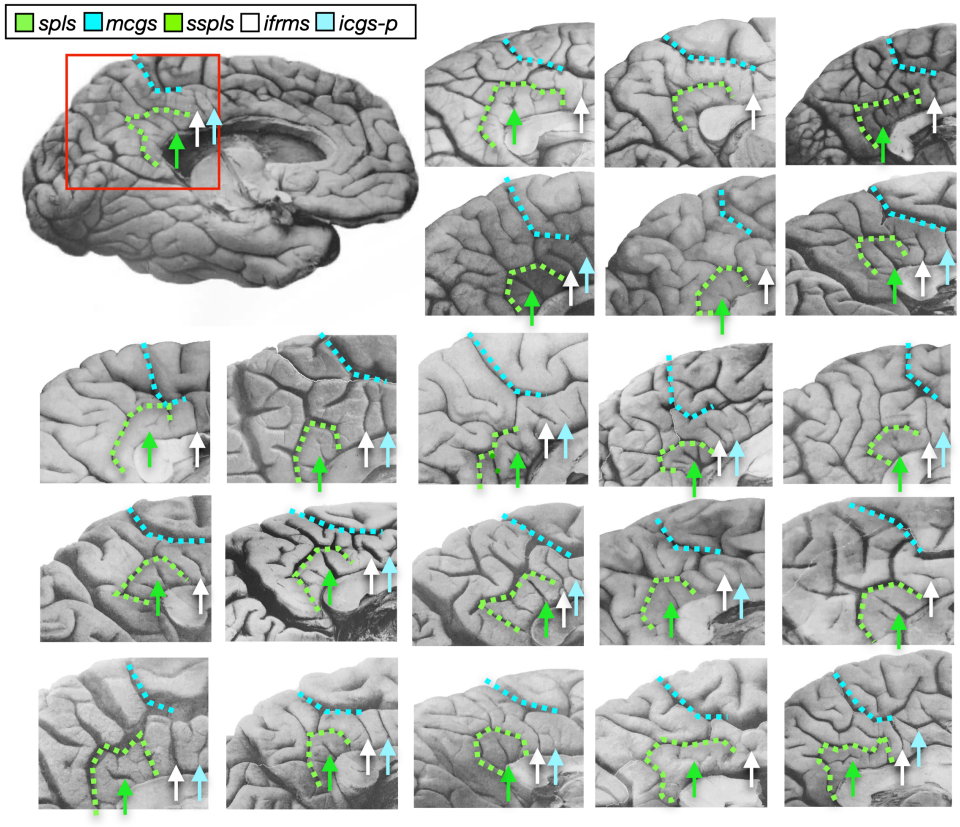

Fig. 3. The *ifrms* is present in postmortem hemispheres. Twenty-two postmortem hemispheres (11 LH and 11 RH) labeled from a classic neuroanatomy atlas (*49*). The *mcgs* and *spls* are labeled with colored dotted lines, while the *ifrms* is identified with a white arrow. When present, the *sspls* and *icgs-p* are identified with green and cyan arrows, respectively. The *ifrms* is present in all hemispheres labeled, while the other two shallow sulci have more variable appearances, which is consistent with our findings from in vivo analyses.

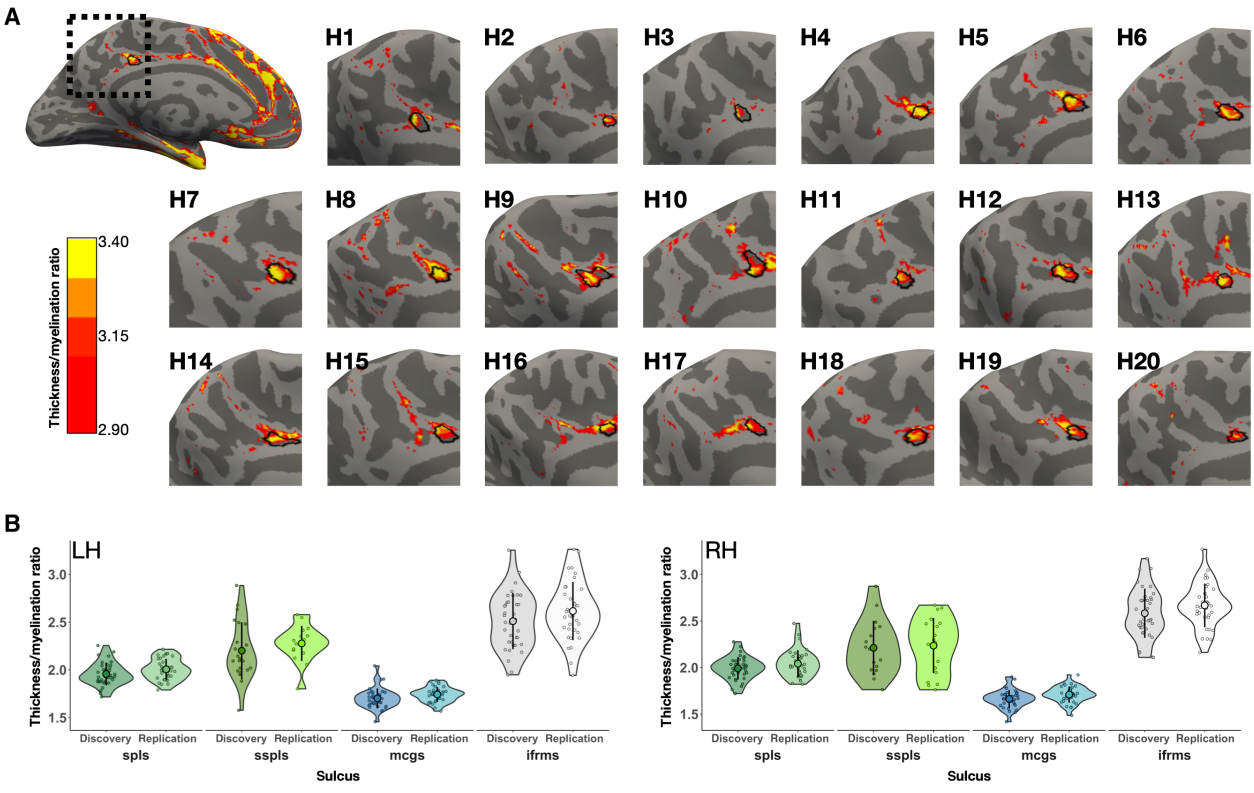

Fig. 4. The *ifrms* is a macroanatomical and microstructural landmark in PCC. (**A**) A sample LH, alongside 10 LH and 10 RH (H1, H2, etc.) zoomed in on the PMC, displaying the thickness/myelination ratio (>2.9) relative to the *ifrms* (outlined in black). The RHs have been mirror-reversed to be in alignment with the LHs. The *ifrms* colocalizes with a portion of PCC that is cortically thick and lightly myelinated. (**B**) Thickness/myelination ratio of two deep PMC sulci (*spls* and *mcgs*) and two shallow PMC sulci below them (*sspls* and *ifrms*, respectively) in the discovery and replication samples in the LH and RH. Individual participants from the discovery and replication samples (small colored circles), means (large colored circles), SD (black line), and kernel density estimate (colored violins) are plotted for each sulcus. Each sulcus is colored according to the legend in Fig. 2A. The difference in the thickness/myelination ratio is much greater ($P < 0.001$) between the anterior deep and shallow sulci (*mcgs* versus *ifrms*) compared to the posterior deep and shallow sulci (*spls* versus *sspls*).

hemisphere (left and right) for each sample. In both samples, we observed a main effect of sulcal type [discovery: $F(1, 249) = 526.4$, $P < 0.001$, $\eta^2G = 0.68$; replication: $F(1, 245) = 682.92$, $P < 0.001$, $\eta^2G = 0.74$)], in which the shallow sulci (*sspls* and *ifrms*) had a larger thickness/myelination ratio—i.e., were thicker and less myelinated—than the deeper sulci (*spls* and *mcgs*); this was true regardless of hemisphere (Fig. 4B). In addition, there was a sulcal type × position interaction in both samples [discovery: $F(1, 249) = 142.14$, $P < 0.001$, $\eta^2G = 0.36$; replication: $F(1, 245) = 186.6$, $P < 0.001$, $\eta^2G = 0.43$], such that the difference in the thickness/myelination ratio was greater in the more anterior PMC, between the *ifrms* and *mcgs*, compared to posterior PMC, between the *sspls* and the *spls*, across hemispheres (P values <0.001, Tukey's adjustment in both samples; Fig. 4B). While previous work in ventral temporal cortex identified relationships among myelin, curvature, and thickness (*52*), this is not necessarily the case across the cortex. For example, regarding the *ifrms*, depth only correlated with the thickness/myelination ratio in the RH of the replication sample ($r = -0.56$, $P = 0.003$, false discovery rate corrected), and cortical thickness did not correlate with myelination in either sample (all r values <0.31, all P values >0.12). Together, the *ifrms* overlaps with a focal PCC cluster that is cortically thick and lightly myelinated across hemispheres and samples.

The ifrms predicts focal, functional regions of the lateral frontoparietal network implicated in cognitive control

Classic (*23*) and recent (*11*, *20*, *21*) findings implicate the organization of tertiary sulci to the functional organization of association cortices. Therefore, we sought to extend this assessment to PMC by examining the relationship between the *ifrms* and functional parcellations of PMC. Specifically, we tested whether the *ifrms* is consistently located within a functional region (axial sulcus) or whether it consistently identifies the boundary, or transition, between regions (limiting sulcus). To achieve this goal, we leveraged resting-state functional MRI (fMRI) functional connectivity parcellations from a recently published study (*41*) for each individual HCP participant. These parcellations were conducted blind not only to cortical folding but also to our sulcal definitions. Figure 5A (left) illustrates the 17-network parcellation on an individual participant's LH (*41*). To quantitatively determine the relationship between cortical network parcellations and sulcal definitions, we created functional connectivity network profiles (termed "connectivity fingerprints") by calculating the overlap between each of the 17 networks within the cortical area of a given sulcus on the native hemisphere via the Dice coefficient (Materials and Methods; Fig. 5A, right) as in our previous work (*21*). We leveraged the functional parcellation in each participant to test whether the *ifrms* is a potential landmark identifying the

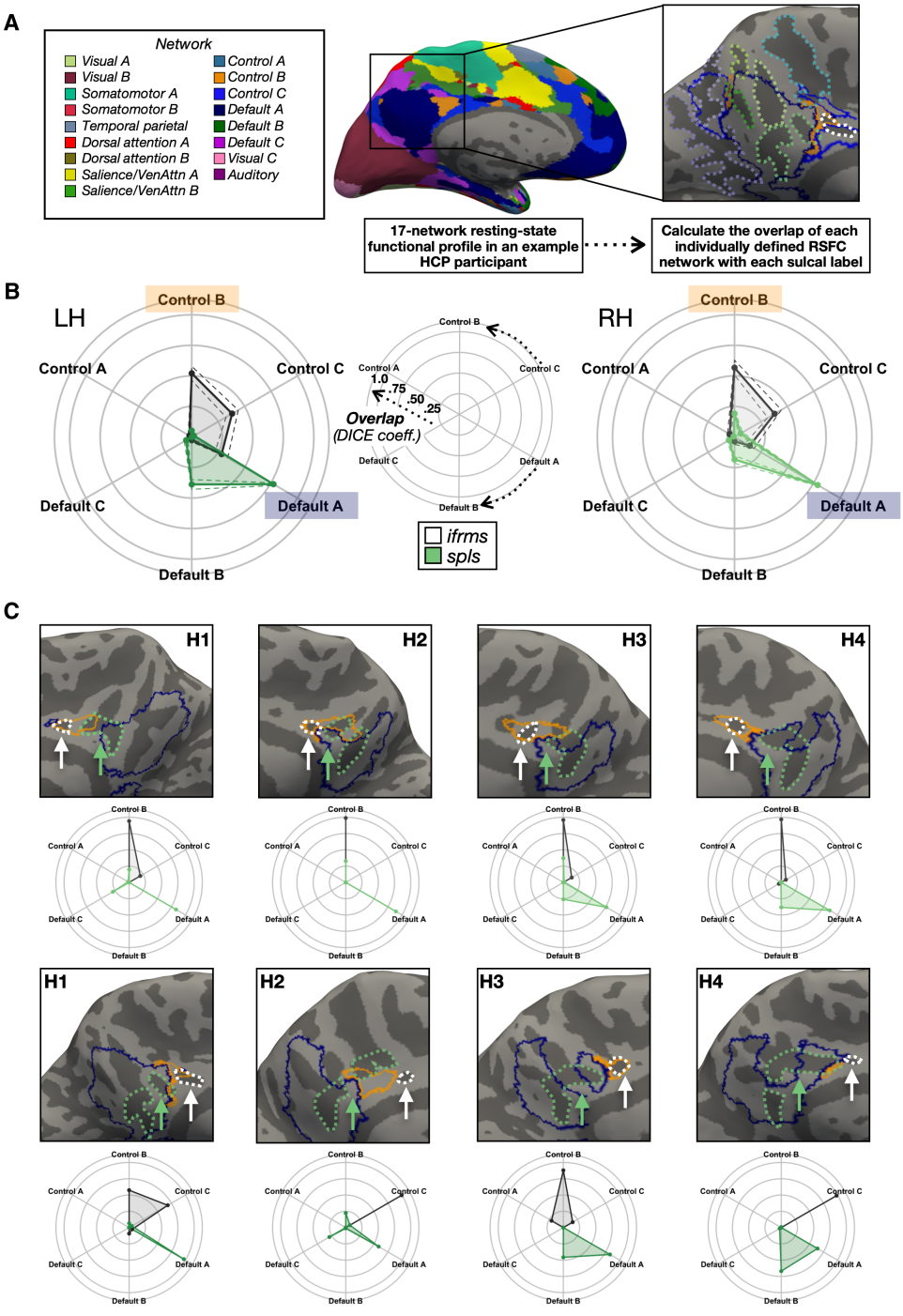

Fig. 5. The *ifrms* is a functional landmark in PCC. (**A**) Schematic of how resting-state functional connectivity (RSFC) profiles were generated for each participant in an example LH. Individual participant RSFC parcellations were obtained from a recent study (*41*), blind to cortical folding, and independent of our sulcal definitions. The connectivity fingerprint represents the overlap of each network within a given sulcal area. (**B**) Polar plots showing the mean connectivity fingerprints of the *ifrms* and *spls* in the LH (left, darker shades) and RH (right, lighter shades) of the discovery sample. Solid lines, mean. Dashed lines, ±1 SEM. Center: Legend for interpreting the polar plots in the left and right images. Arrows denote the direction of each network's overlap (cognitive control, top; default mode, bottom). The closer to the periphery of the circle, the higher the Dice coefficient. (**C**) Connectivity fingerprints for both the RH (top) and LH (bottom) from four individual hemispheres relative to cortical surface reconstructions with CCN-b (orange) and DMN-a (blue) outlines. *Ifrms* (white) and *spls* (green) outlines are also included as dotted lines and designated with arrows. The *ifrms* overlaps primarily with CCN-b and CCN-c regions, while the *spls* overlaps more with DMN-a and DMN-b regions with between-hemisphere differences in the different samples (see figs. S8 and S10 for all participants).

CCN, while the more posterior *spls* is a potential landmark identifying the DMN (see figs. S8 and S10 for connectivity fingerprints of all participants; see the Supplementary Materials and fig. S11 for connectivity fingerprints of the three *prcus*).

Consistent with our hypothesis, the *ifrms* predicted the location of CCN regions, while the *spls* predicted the location of DMN regions in both discovery and replication samples. In both samples, a three-way repeated measures (rm)–ANOVA with factors sulcus (*spls* and *ifrms*), network (CCN-a, -b, and -c, and DMN-a, -b, and -c), and hemisphere (left and right) yielded a sulcus × network interaction [discovery: $F(5, 175) = 94.71$, $P < 0.001$, $\eta^2G = 0.41$; replication: $F(5, 165) = 52.75$, $P < 0.001$, $\eta^2G = 0.31$] and a sulcus × network × hemisphere interaction [discovery: $F(5, 175) = 3.27$, $P = 0.007$, $\eta^2G = 0.02$; replication: $F(5, 165) = 8.51$, $P < 0.001$, $\eta^2G = 0.04$; see the Supplementary Materials]. Post hoc analyses in both samples showed that the shallow *ifrms* overlapped significantly more with regions CCN-b and CCN-c than with DMN regions (*P* values <0.001, Tukey's adjustment; Fig. 5B and figs. S8 to S10), while the *spls* overlapped significantly more with DMN-a and DMN-b than CCN regions (*P* values <0.001, Tukey's adjustment; Fig. 5B and figs. S8 to S10).

To directly quantify the location of the *ifrms* relative to CCN regions, we performed linear regressions in each hemisphere between *ifrms* coordinates and coordinates of CCN subregions (CCN-b, CCN-c; Figs. 5 and 6 and figs. S8 to S10). *Ifrms* coordinates were predictive of coordinates of CCN regions in both discovery and replication samples (table S7 for CCN-b and table S8 for CCN-c). Specifically, the more anterior and superior the *ifrms*, the more anterior and superior the CCN-b (Fig. 6B) and CCN-c (Fig. 6C) regions. This structure-function correspondence is impressive given the relatively small surface area of both the *ifrms* (average surface area ± SD = 77.86 ± 35.83 mm^2)

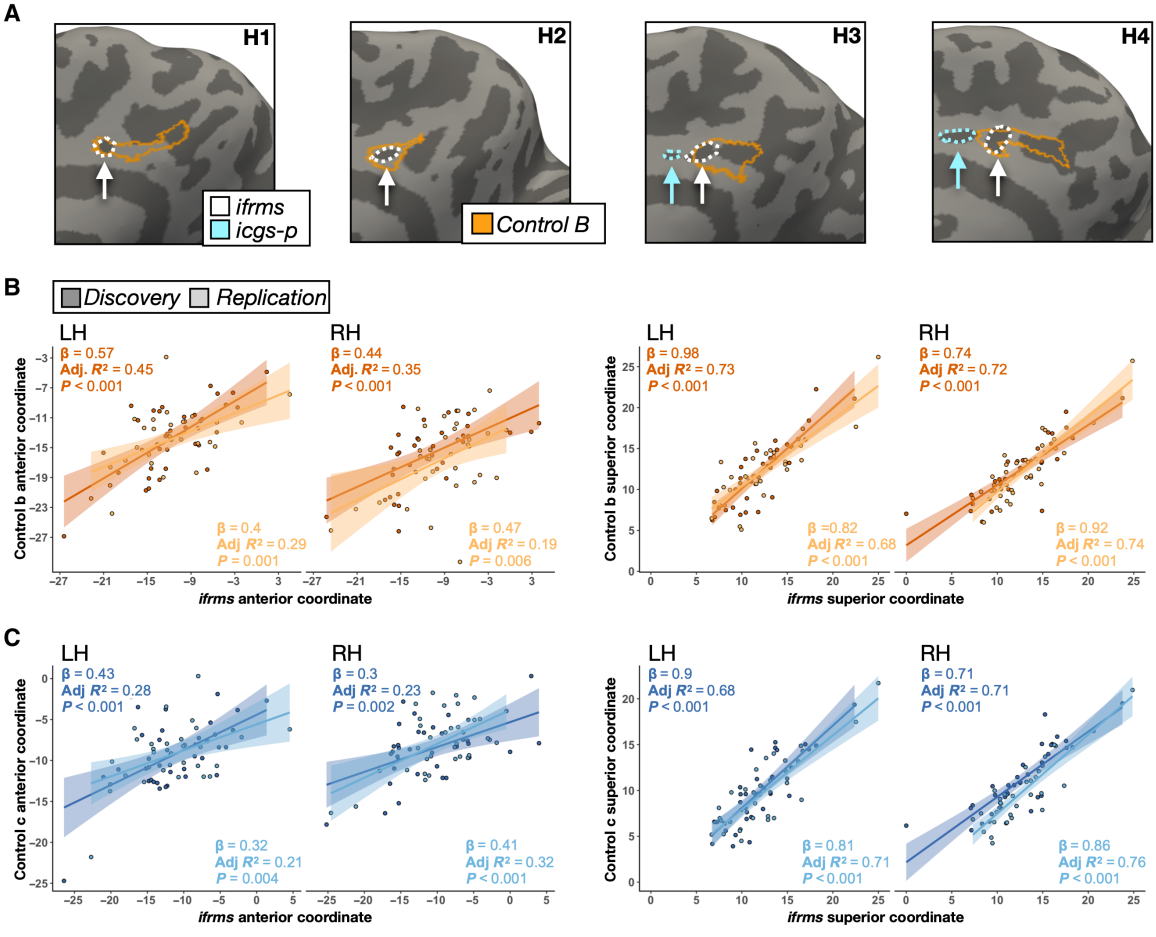

Fig. 6. Individual differences in the location of cognitive control regions correlates with variability in the sulcal anatomy. (**A**) Four example individual RHs from the discovery sample (two without and two with the *icgs-p*) illustrating the qualitative relationship between the *ifrms* and functionally defined CCN-b (outlined in orange) by Kong and colleagues (*41*). The *ifrms* (white) and *icgs-p* (cyan) are outlined and indicated with an arrow. (**B**) Linear models (lm) capturing the relationship between the *ifrms* and CCN-b in individual participants (colored circles), from the discovery (dark orange) and replication (light orange) samples, for their mean anterior (left) and superior (right) coordinates for each hemisphere. The best fit line from the regression and ±95% confidence interval are color-matched to each sample. Results for each lm are in the top left corner (slope, adjusted R^2, and *P* value), as well as in table S7. (**C**) Same as (B), but between the *ifrms* and cognitive control network C (CCN-c; table S8) for both the discovery (dark blue) and replication (light blue) samples. The anterior and superior mean coordinates of the *ifrms* and CCN-b and CCN-c are strongly correlated with one another, indicating that variability in the location of the functional CCN-b and CCN-c regions across individuals also correlates with variability in the sulcal anatomy.

and the CCN-b (average surface area ± SD = 147.53 ± 125.23 mm^2) compared to the larger CCN-c (average surface area ± SD = 390.34 ± 124.94 mm^2).

The *ifrms*-functional correspondence not only is specific to the parcellation by Kong and colleagues (*41*) but also extends to other individual participants and a different functional parcellation from the Midnight Scan Club (MSC; see the Supplementary Materials and figs. S12 to S14 for further details), which identifies two regions ("parietal memory" and "frontoparietal") adjacent to the DMN hub in PCC (*42*). Across parcellations, each region is functionally connected to areas in similar cortical locations. Specifically, the CCN-b and CCN-c regions that colocalize with the *ifrms* are connected to dorsal PRC, medial prefrontal cortex (PFC), lateral PFC (LPFC), lateral parietal, and lateral temporal regions, while the frontoparietal and parietal memory regions of the MSC are also connected to dorsal PRC, medial PFC, LPFC, lateral parietal, and lateral temporal regions (*41*, *42*). In addition, this structure-function relationship is not limited to analyses conducted in individual participants; it also generalizes to meta-analyses using Neurosynth (*44*). When projecting Neurosynth meta-analysis maps to the MNI2009b surface, we found that the *ifrms* (fig. S15A) corresponds to the location of a small cluster for the terms "cognitive control" and "frontoparietal network" ventral to the DMN hub across hundreds of studies consisting of thousands of participants (fig. S15B). In addition, further considering a combinatory meta-analysis across association terms suggested by a recent preprint from OHBM WHATNET [cognitive control, frontoparietal, executive, demand (proxy for multiple demand), and domain general] (*45*), there was a focal cluster neighboring the DMN hub that overlapped with the *ifrms* with variable convergence across these terms (fig. S15C). Together, these analyses indicate that the *ifrms* colocalizes with a focal, functional region neighboring a large hub of the DMN in PCC across parcellations in individual participants and meta-analyses averaged across hundreds of studies (see the Supplementary Materials for further details on these analyses). Despite variability in parcellations and the names of the PCC region underneath the *mcgs*, the commonality shared across parcellations and analysis approaches is that this region is considered part of the lateral frontoparietal network and is implicated in cognitive control.

The *ifrms* is present in human PCC across the life span but is variably present in chimpanzees across age groups

Recent research indicates that some tertiary sulci are also identifiable in nonhuman hominoids, while others are more variable in nature (*11*, *53*, *54*). Thus, we further tested whether the *ifrms* is identifiable in nonhuman hominoids in different age groups—and, if so, to compare sulcal depth and cortical thickness of the *ifrms* across age groups and species as shallowness and thickness are defining features of the *ifrms*. To do so, we combined the two young adult samples from the previous section into one group ($N = 72$; age, range = 22 to 36; average ± SD = 29.06 ± 3.59). We then defined the 8 to 11 PMC sulci in a juvenile human dataset ($N = 72$; age, range = 6 to 18; average ± SD = 11.89 ± 3.53) and a healthy older human dataset ($N = 72$; age, range = 64 to 90; average ± SD = 74.49 ± 5.15), both composed of 72 participants. Last, we labeled the *ifrms*—when present—in 60 chimpanzee participants (age, range = 9 to 51; average ± SD = 23.16 ± 9.75), which we also binned into age groups similar to humans: juvenile (age <22), young adult (22 ≤ age ≤ 36), and older adults (age > 36; Fig. 7A).

In humans, the *ifrms* was identifiable in every hemisphere examined in juveniles and healthy older adults, as in young adults (Fig. 7B and tables S9 and S10). Cortical locations (see fig. S16 for all 1423 sulcal definitions in juvenile human hemispheres and fig. S17 for all 1386 defined PMC sulci in healthy elderly human hemispheres) were similar to those in the young adult sample, and the sulcal intersections (tables S11 to S14) were highly correlated within and between age groups (all rs > 0.60 and all Ps < 0.001; fig. S18). Contrary to the consistent identification of the *ifrms* in humans across age groups, the *ifrms* was identifiable in about half [LH: 50% (30 of 60); RH: 46.67% (28 of 60)] of the chimpanzees across age groups (Fig. 7B; fig. S19 for all 120 chimpanzee hemispheres).

Morphologically, normalized sulcal depth (Materials and Methods) of the *ifrms* is shallower in chimpanzees than in humans and differs by age group. Specifically, a three-way ANOVA with factors hemisphere (left and right), age group (juvenile, young adult, and older), and species (human and chimpanzee) yielded three significant effects. First, there was a main effect of species [$F(1, 475) = 6.85$, $P = 0.01$, $\eta^2G = 0.01$], wherein the *ifrms* was deeper in humans than in chimpanzees (Fig. 7C; fig. S20A for unnormalized data). Second, there was a main effect of age group [$F(2, 475) = 10.68$, $P < 0.001$, $\eta^2G = 0.04$], such that the *ifrms* was deeper in the juvenile and older age groups than in the younger adult group (Fig. 7C). Third, there was a main effect of hemisphere [$F(1, 475) = 15.43$, $P < 0.001$, $\eta^2G = 0.03$], wherein the *ifrms* was generally deeper in the LH compared to the RH (Fig. 7C).

In addition, the *ifrms* was relatively cortically thinner in chimpanzees compared to humans across age groups. A three-way ANOVA with hemisphere (left and right), age group (juvenile, young adult, and older), and species (human and chimpanzee) as factors yielded main effects of age group [$F(2, 475) = 135.37$, $P < 0.001$, $\eta^2G = 0.36$] and species [$F(1, 475) = 63.59$, $P < 0.001$, $\eta^2G = 0.12$]. There was also a hemisphere × species interaction [$F(1, 475) = 6.98$, $P = 0.009$, $\eta^2G = 0.01$], such that the *ifrms* in chimpanzees was thicker in the RH (Fig. 7D; fig. S20B for unnormalized data). Last, in our historical analyses, we were also able to identify the *ifrms* in a subset of postmortem chimpanzee hemispheres, as well as in other nonhuman hominoids (gorillas and orangutans). In addition, we were able to identify a shallow "dimple" in the same location of the brain (which we refer to as the inframarginal dimple, *ifrmd*) in Old World and New World monkeys (see the Supplementary Materials and fig. S21), which is consistent with references to a posterior cingulate dimple in modern research mentioned earlier in these results (fig. S1). We provide the sulcal depth (in millimeters), surface area (in square millimeters), and thickness (in millimeters) values (average ± SD) for all 11 PMC sulci across age groups in the Supplementary Materials (fig. S22 and tables S15 to S17).

Last, considering that tertiary sulci are often classified on the basis of their presence or prominence—for example, the paracingulate sulcus (*pcgs*) is defined as "absent," "present," or "prominent" on the basis of length [a criterion developed by Yucel *et al.* (*55*)]—we leveraged a data-driven approach to classify the *ifrms* using k-means clustering on the primary descriptive features of tertiary sulci (depth and surface area; Fig. 2 and fig. S22) (*11*, *21*, *22*, *39*) across age groups and species. This approach revealed that the morphology clustered the *ifrms* into two groups in both hemispheres (fig. S23). These two groups and group centers (fig. S23) can be used in future work to differentiate a present *ifrms* and a prominent *ifrms* and reveal whether these different classifications relate to brain function, behavior, and disease—as done previously for different characterizations of the *pcgs* [for example, see (*15*, *16*, *19*)].

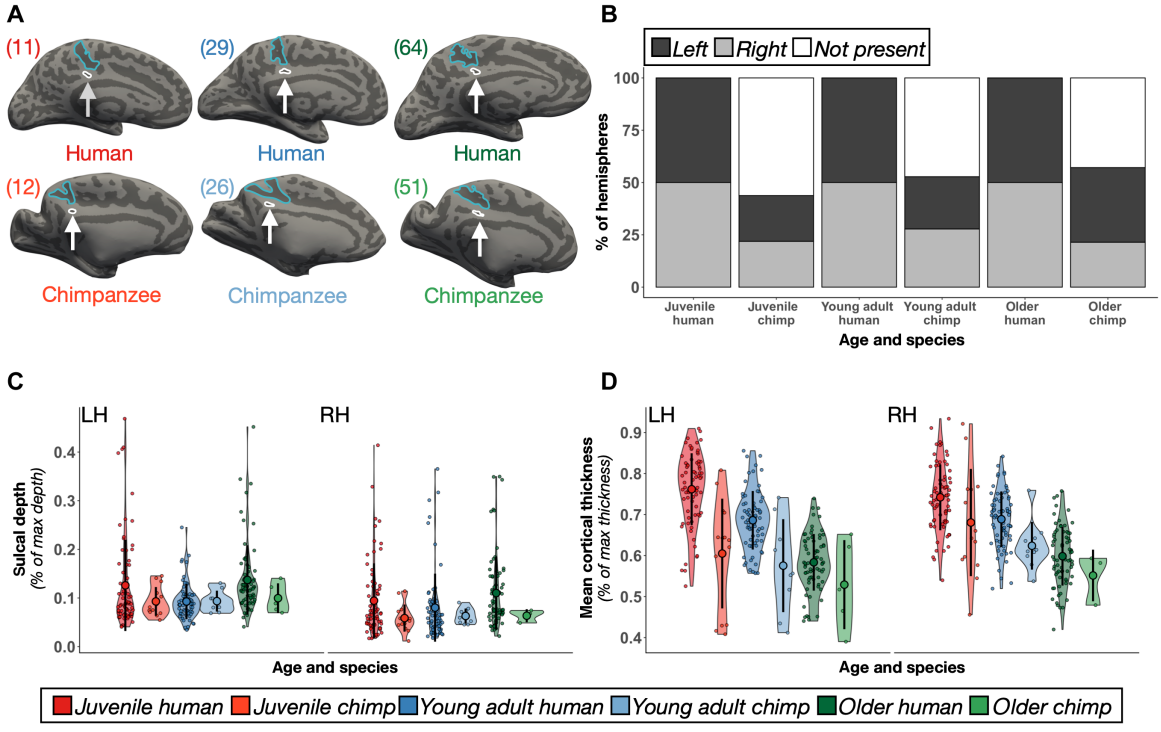

Fig. 7. The *ifrms* across species and age groups. (**A**) Six example LHs identifying the *ifrms* across age groups (left to right: juvenile, young adult, and older adult) and species (top, human; bottom, chimpanzee; cortical surfaces are not to scale). The *ifrms* (white) is outlined and labeled with an arrow below the *mcgs* (blue) in each participant. Ages are in the top left corner of each hemisphere. (**B**) The percent of hemispheres with the *ifrms* binned by species and age group. LH, dark gray; RH, light gray; White, absent. The *ifrms* is present in every human, but not chimpanzee, hemisphere measured across age groups. The *ifrms* is only present in about half of chimpanzee hemispheres [juveniles: LH, 43.75% (14 of 32); RH, 43.75% (14 of 32); young adults: LH, 50% (9 of 18); RH, 55.56% (10 of 18); older adults: LH, 71.43% (5 of 7); RH, 42.86% (3 of 7)]. (**C**) Normalized sulcal depth (% of max depth) of the *ifrms* across age groups and between species plotted for each individual participant in each hemisphere. The mean (large colored circles), SD (black line), and kernel density estimate (colored violin) are also plotted for each sulcus. Each age group and species combination is colored according to the legend. The *ifrms* is deeper in humans compared to chimpanzees and in older adults and juveniles than in young adults across species. (**D**) Same layout as (C) but for normalized cortical thickness (% of max thickness). The *ifrms* shows an age- and species-related decrease in thickness.

Tools to automatically define the *ifrms* using convolutional neural networks

As the *ifrms* is a new tripartite landmark in PCC and because of its prominence across age groups and species, we have created freely available tools to predict the *ifrms* in new datasets. We used recently developed (Materials and Methods) (*56*) spherical convolutional neural networks (CNNs) with context-aware training on the eight PMC sulci identified in the young adult participants. We then quantified the correspondence between the predicted and actual sulcal labels. Here, we report the performance for the *ifrms*; we include the performance for all sulci in the Supplementary Materials.

We found that spherical CNNs were more accurate [$t(71) = -3.69$, $P < 0.001$, $d = -0.435$] at predicting the *ifrms*' location than more traditional cortex-based alignment (CBA) tools (average ± SEM; CNN: 0.61 ± 0.03; CBA: 0.5 ± 0.02; Fig. 8A). The Dice values of the CNN labels were skewed toward higher values, emphasizing that CNNs accurately labeled the *ifrms* most of the time (Fig. 8B, bottom left). This variable performance likely occurred because the *ifrms* is small in surface area and highly variable from one hemisphere to the next. Thus, the CNN will pinpoint an area in which the *ifrms* will be located and present tools still require manual intervention. Nevertheless, with additional definitions of the *ifrms* that are then added to our shared tools (in the spirit of citizen science), the automatic definition of the *ifrms* and of tertiary sulci more broadly given our recently shared tools should vastly improve (*56*). In addition, while the *ifrms* was, as expected, not as predictable as the larger, deeper primary sulci (*pos*, *mcgs*, and *spls*), the *ifrms* was as predictable as the precuneal-limiting sulcus (*prculs*) and even more predictable than the three *prcus* sulci, which were also deeper and larger than the *ifrms* (fig. S24). The efficacy of this automated approach speaks to the anatomical consistency of the *ifrms* across individuals. Free dissemination of these tools will expedite the amount of time it takes to define PMC sulci in individual hemispheres in future studies.

DISCUSSION

Here, we examined the functional significance of the PMC sulcal organization, focusing on a newly characterized tertiary sulcus: the *ifrms*. We report five main findings. First, the *ifrms* is identifiable in every human hemisphere in children, young adults, and elderly adults. Second, the *ifrms* is a macroanatomical and microstructural landmark, with the largest thickness/myelination ratio of all PMC sulci. Third, most of the time, the *ifrms* functions as an axial sulcus located within a region of the cognitive control or lateral frontoparietal network, and in some individuals, it overlaps with the dorsoanterior tail of the larger hub of the DMN. Fourth, the *ifrms* is present in some, but not all, nonhuman hominoid hemispheres and appears as a shallow dimple (*ifrmd*) in some nonhuman primate hemispheres. Fifth,

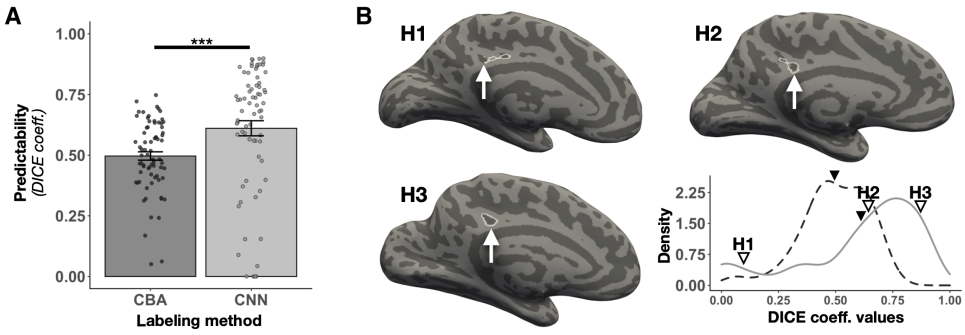

Fig. 8. Automatically defining the *ifrms* using deep learning algorithms. (**A**) Overlap (Dice coefficient) between predicted and manual location of the *ifrms* for cortex-based alignment (CBA) and spherical convolutional neural network (CNN) methods. Bars represent average values, and the error bars indicate ±1 SEM. Circles represent each individual. Asterisks indicate statistically significant differences between the two approaches (***$p < 0.001$). (**B**) Lower right: The density distribution of the *ifrms* Dice coefficient values for the CBA and CNN approaches. The dashed and solid lines represent the CBA and CNN distributions, respectively. The line for each method is colored the same as in (A). The mean Dice coefficient value is visualized with the solid black triangle for each method (CBA = 0.5, CNN = 0.61). In addition, the Dice coefficient values of three individual participants with the CNN approach (indicated by H1, H2, and H3) are identified with outlined triangles (left to right): low accuracy (H1; Dice = 0.09), mean accuracy (H2; Dice = 0.64), and high accuracy (H3; Dice = 0.87). The three participants' corresponding LHs (indicated by H1, H2, and H3) are provided to visually illustrate the differing degrees of overlap between the automated CNN labels and the manual labels. The automated *ifrms* labels are outlined in white, while the manual *ifrms* labels are identified with a white arrow. These data show that the *ifrms* is more accurately defined using the novel CNN approach, and importantly, in most hemispheres, the automated labels coincided strongly with the manual labels.

morphological features of the *ifrms* differ across age groups and between species. In the following sections, we discuss these findings in the context of (i) the *ifrms* as a tripartite landmark, (ii) tertiary sulci in cortical development and evolution, (iii) general limitations and future directions of the present study, and (iv) translational applications of tertiary sulci.

We refer to the *ifrms* as a tripartite landmark because it identifies a cortically thick and lightly myelinated portion of PCC, as well as a functional region of the lateral frontoparietal network implicated in cognitive control. In classic neuroanatomical terms (*7*), then, the *ifrms* is an axial sulcus as it cooccurs with a particular cortical area rather than identifies a transition between areas (limiting sulcus). Examining classic and recent microstructural (*57*, *58*) and multimodal parcellations in PCC (*43*) shows that the axial definition of the *ifrms* also likely applies to cytoarchitectonic and multimodal areas, which can be explored in future studies (fig. S25) (*59*).

The present findings build on a growing body of work examining the morphological, functional, and cognitive features of tertiary sulci across age groups and species (*13*, *15*–*19*, *21*, *22*, *53*, *54*). Developmentally, our results extend previous work showing that morphological features of tertiary sulci in other cortical expanses predict performance on different cognitive tasks. For example, the depths of tertiary sulci in LPFC robustly predict reasoning skills in a developmental cohort (*22*). In addition, the morphology of the *pcgs* predicts individual differences in cognition (*15*–*17*, *19*) and whether individuals with schizophrenia will hallucinate or not (*18*). Future studies may identify that morphological features of the *ifrms* may predict behavior and cognition.

Evolutionarily, the present work adds to the growing comparative neuroscience literature classifying the presence/absence of tertiary sulci across species. For example, the *mfs* was identifiable in every human and nonhuman hominoid hemisphere examined (*53*), while the *pcgs* was more variable across species (*54*). Thus, tertiary sulci are not always identifiable in association cortices, further highlighting the impressive fact that the *ifrms* is identifiable in all hemispheres measured across age groups in humans. Future studies will further assess the prevalence of tertiary sulci among humans and across species in other cortical expanses.

In addition to assessing the incidence of tertiary sulci in a given cortical expanse, future studies could determine whether the presence or absence of a tertiary sulcus directly affects the structure or function of that cortical expanse, as well as individual differences in the variability of this relationship. For example, in terms of consistency, this structural-functional coupling generalized across analysis types (individual participant analyses, as well as group and meta-analyses) and different functional parcellations of PCC. Complementing this consistency, the variability we observed may reflect individual differences in the location and morphology of the *ifrms* relative to recently identified connector "hubs" that integrate information between CCNs and DMNs or between different CCNs, which would be critical for integrating information between networks (*60*). Thus, this variability may further suggest that the small functional regions overlapping the *ifrms* may contain subpopulations of neurons that vary in their task-active and task-negative activity levels, which can be tested in future research. In addition, considering that primate PCC is implicated in cognitive control (*30*, *61*, *62*) and also has area 23d (*63*), future research can test whether the variably present primate *ifrmd* corresponds to either of these features.

A main limitation of the present work is that the *ifrms* and other tertiary sulci must be manually defined, as they are not included in present approaches that automatically identify most primary and secondary sulci. The main benefit of manual definitions is their precision at the level of individual participants, which allows the most accurate assessment of individual differences in both morphological features themselves and the relationship between morphological features and functional or cognitive significance. This precision also helps dispel a historical trend in the field of neuroanatomy—the attempt to describe how the brains of geniuses are "unique" [e.g., Einstein (see the Supplementary Materials)]. The sulcal patterning of these brains is often within the normal range of interindividual variability when considering tertiary sulci (see the Supplementary Materials and fig. S26). However, manual sulcal definitions are slow and arduous,

which typically limits sample sizes. For example, while this study includes the manual definition of more than 4000 sulci, it only includes 572 hemispheres—a large number for an anatomy study, but a relatively small one for studies exploring the neural basis of individual differences in cognition, functional brain organization, or neurological conditions.

To expedite the labeling process, we benchmarked deep learning algorithms to automatically identify eight of the manually defined PMC sulci, including the *ifrms* (Fig. 7 and fig. S24). As we share our deep learning methods (https://github.com/ilwoolyu/SphericalLabeling), these tools can be used in future studies focused not only on tertiary sulci in PMC but also throughout the cerebral cortex. By expediting sulcal labeling, such methods will facilitate the analysis of larger sample sizes in the service of elucidating the functional significance of variability in tertiary sulci across individuals.

With regard to sulcal classifications, we have classified the novel sulci in this study (*ifrms, sspls,* and *icgs-p*) as putative tertiary sulci based on their morphology (small surface area and shallow depth). However, tertiary sulci are truly classified on the basis of when they emerge during gestation, which is around 36 weeks (*2*, *3*, *13*, *20*, *23*, *40*, *64*, *65*). Therefore, to determine whether these sulci are definitively tertiary, future work can seek to identify when exactly they emerge in gestation. Furthermore, to shed light on the relationship between the cross-sectional morphological differences observed here across age groups, future work should quantify the longitudinal interrelations among morphological, microstructural, and functional features of the *ifrms* and other overlooked sulci.

While it is unlikely that all tertiary sulci will serve as landmarks in association cortices, it is important to know which ones do, especially because recent work shows that the morphology of tertiary sulci relates to the symptomatology of several disorders. For example, Garrison *et al.* (*18*) showed that the length of the *pcgs* increased the likelihood of hallucinations in individuals with schizophrenia. In addition, Brun *et al.* (*66*) showed that the deepest points within a tertiary sulcus in LPFC were different in individuals with autism spectrum disorder (ASD) compared to NT individuals. The authors also identified correlations between the depth of these tertiary sulcal points and social communication impairments in ASD individuals (*66*). Last, Ammons *et al.* (*67*) recently identified morphological differences in *mfs* morphology between ASD and NT individuals. In addition, *mfs* morphology correlated with the ability of ASD individuals to interpret emotions and mental states from facial features (*67*). As such, future studies can build on the findings from our present work to determine whether morphological features of PMC tertiary sulci also have translational applications. For example, there is a considerable amount of research implicating the PMC, and the functional networks within PMC, in Alzheimer's disease, ASD, attention deficit hyperactivity disorder, depression, and schizophrenia (*32*, *68*).

In conclusion, through the definition of 4511 sulci in 572 hemispheres, we not only established a comprehensive description of the sulcal anatomy of human PMC but also identified a novel sulcus—the *ifrms*—that serves as a tripartite landmark in PCC. Methodologically, this study lays the foundation for a myriad of potential PMC and PCC research—whether that be relating the sulci characterized in this study to other anatomical features, additional functions, behavior, or the many disorders that affect this cortical expanse. Evolutionarily and developmentally, morphological analyses between age groups and species show that unique properties of this cortical indentation differ across the life span and between species. Theoretically, our findings support Sanides' classic hypothesis that tertiary sulci may serve as landmarks within association cortices (*23*). Last, considering that neuroanatomists have been charting and labeling the outer surface of the human cerebrum for centuries, it is unusual that a sulcus that is observed so consistently across humans was never extensively studied until now. This begs the question: How many other sulci have we yet to uncover?

MATERIALS AND METHODS

We describe our methodological approach in three separate sections. The first describes the methods implemented in the main portion of our study examining the anatomical and functional features of sulci in the human PCCs and PRCs in a young adult cohort, in separate discovery and replication samples. The second focuses on the novel *ifrms* and describes the cross-sectional methods implemented to compare the morphological features of the *ifrms* across different age groups (juveniles, young adults, and older adults) and species (humans and chimpanzees). The third details the statistical methods used for the analyses in the previous two sections.

Examining anatomical and functional features of sulci in the human PCC and PRC in young adults

Participants

Data for the young adult cohort analyzed in the present study were from the freely available HCP database (https://humanconnectome.org/study/hcp-young-adult) (*69*). The discovery dataset consisted of the first five numerically listed HCP participants and a random selection of 31 additional participants (17 females and 19 males) whose ages were between 22 and 36 years (average ± SD = 28.97 ± 3.78). These participants were the same as those used in a previous study examining the anatomical and functional features of sulci within LPFC (*21*). The replication sample consisted of 36 additional participants (19 females and 17 males) randomly selected from the HCP database, with a comparable age range (average ± SD = 29.13 ± 3.44, $P = 0.84$). These data were previously acquired using protocols approved by the Washington University Institutional Review Board.

Imaging data acquisition

Anatomical T1w MRI scans (0.7-mm voxel resolution) were obtained in native space from the HCP database, along with outputs from the HCP-modified FreeSurfer pipeline (v5.3.0) (*70*–*73*). Additional details on image acquisition parameters and image processing can be found in Glasser *et al.* (*73*). Maps of the ratio of T1w and T2w scans, which is a measure of tissue contrast enhancement related to myelin content, were downloaded as part of the HCP "Structural Extended" release. All subsequent sulcal labeling and extraction of anatomical metrics were calculated from the cortical surface reconstructions of individual participants generated through the HCP's custom modified version of the FreeSurfer pipeline (*73*).

Anatomical analyses

Macroanatomical boundaries of the PCC and PRC within PMC. On the basis of previous work, there is extensive variability regarding how PCC and PRC are defined (Fig. 1). Here, we defined the PRC by the following posterior, inferior, and anterior boundaries, respectively, in the medial parietal cortex, as shown in Figs. 1 and 2A (left): (i) the parieto-occipital sulcus (*pos*), (ii) *spls*, and (iii) *mcgs*, respectively. While the *spls* nomenclature is used by Vogt *et al.* (*57*, *74*) and our group, because of its typical location superior to the splenium of the corpus callosum, this sulcus is also known as the subparietal

sulcus (*sbps*) (*30*, *40*). Nevertheless, we adopt the *spls* nomenclature because there is an additional shallow sulcus in PCC underneath the *spls* (expanded on further below), which we refer to as the *s-spls* (as opposed to sub-*sbps*). We define PCC as the posterior portion of the cingulate gyrus bounded inferiorly by the callosal sulcus (*cas*), superiorly by the *cgs*, *mcgs*, and the *spls*, and posteriorly by the *pos*.

PCC and PRC sulci. On the basis of the most recent and comprehensive atlas of sulcal definitions throughout the cerebral cortex (*40*), we consider 11 sulci that are either bounding or located within PCC and PRC. In addition to the *pos*, *spls*, and *mcgs* as mentioned in the previous section, which bound the PRC, we also defined five sulci within the PRC: the *prculs*, the superior parietal sulcus (*sps*), and three *prcus* (*prcus-p*, *prcus-i*, and *prcus-a*). The *prculs* branches off of the superior portion of the *pos* within the posterior PRC. The *sps* is located within the medial portion of the superior PRC and often extends into superior portions of lateral parietal cortex [for additional morphological information on the *sps*, see (*48*)]. While previous research identifies a single *prcus* (*46*) or includes three in their schematic, but only explicitly labels one component as the *prcus* (*40*, *48*), we reliably identified three different *prcus*—often intersecting in different combinations with the *spls*, *mcgs*, and *sps* [the latter intersection replicating "Subtype e" described in (*48*)], and each other (tables S3, S5, S11, and S13). Because we can identify each sulcus in every hemisphere, we propose the following labels for these sulci [mirroring the labeling approach for the three components of the posterior middle frontal sulci (*40*)]: (i) *prcus- p*, (ii) *prcus-i*, and (iii) *prcus-a*.

In addition to these eight sulci, we also considered three shallow PCC sulci. Past research has referred to these indentations in a variety of ways, typically referring to them as inconsistent dimples or as branches of the *cas* or *cgs* (fig. S1), and most recently identifying an intracingulate sulcus in the middle portion of the cingulate gyrus (*47*). We consistently identify a shallow sulcus in every hemisphere. As this sulcus is always inferior to the *mcgs*, we label it the *ifrms*. We also identify two tertiary sulci anterior and posterior to the *ifrms* in a subset of individuals and hemispheres. Posteriorly, a variable sulcus is sometimes present inferior to the *spls*, which we label the *sspls*. Anteriorly, a variable sulcus is also sometimes present, which we refer to as the *icgs-p*. We suggest this label because while a recent study suggests labeling an intracingulate sulcus (*47*), our data in individual participants indicate that there are many intracingulate sulci, which necessitates more precise labels discriminating these sulci from one another.

Sulcal labeling. Each PCC and PRC sulcus was manually defined within each individual hemisphere on the FreeSurfer inflated mesh with tools in tksurfer as described in our previous work (*21*, *22*). Specifically, the curvature metric in FreeSurfer distinguished the boundaries between sulcal and gyral components, and manual lines were drawn to separate sulcal components and the appearance of sulci across the inflated, pial, and smoothwm surfaces. The sulcal labels were generated using a two-tiered procedure. The labels were first defined manually by trained raters (E.H.W., B.J.P., and T.H.) and then finalized by a neuroanatomist (K.S.W.). In each hemisphere, we first labeled the more stable sulci bounding the PCC and PRC (e.g., *pos*, *spls*, *mcgs*), and then we identified the remaining sulcal components within the PCC and PRC. All anatomical labels for a given hemisphere were fully defined before any morphological or functional analyses of the sulcal labels were performed.

Extracting anatomical features from sulcal labels. After all sulci were defined, anatomical features [sulcal depth (in millimeters), cortical thickness (in millimeters), surface area (in square millimeters), and myelination (T1w/T2w ratio)] were extracted. Raw millimeter values for sulcal depth were calculated from the sulcal fundus to the smoothed outer pial surface using a custom-modified version of a recently developed algorithm building on the FreeSurfer pipeline (*75*). Although classic work in postmortem brains by Ono *et al.* (*46*) did not identify all PMC sulci included in the present study, three sulci (*pos*, *spls*, and *cgs*) overlapped between the two studies and displayed similar ranges for sulcal depth (Supplementary Materials). Mean cortical thickness (in millimeters) and surface area (in square millimeters) were extracted from each sulcus using the built-in mris_anatomical_stats function in FreeSurfer (*76*). Average values for myelination were obtained using an in vivo proxy for myelination: the T1w/T2w ratio for each individual hemisphere available in the HCP dataset (*77*).

Quantitative assessment of incidence rates of PCC and PRC tertiary sulci. To compare the incidence rates of tertiary sulci (*ifrms*, *icgs-p*, and *sspls*) in PCC and PRC, chi-squared tests were implemented, along with follow-up post hoc pairwise comparisons.

Qualitative labeling of PCC and PRC sulci in postmortem hemispheres. To assure that our labeling of PCC and PRC sulci was not an artifact of the cortical surface reconstruction process, we also identified PCC and PRC sulci within postmortem human brains (22 hemispheres total) from a classic neuroanatomy atlas (*49*). Critically, the *ifrms* was present 100% of the time.

Quantitative assessment of PMC sulcal depth. We quantitatively compared PMC sulcal depth using a two-way ANOVA with sulcus (*pos*, *spls*, *mcgs*, *sspls*, *ifrms*, and *icgs-p*) and hemisphere (left and right) as factors.

Quantitatively assessing the macroanatomical and microanatomical properties of PMC sulci along an anterior-posterior dimension. To quantitatively assess how macroanatomical (cortical thickness) and microanatomical (myelination) features of PMC sulci vary along an anterior-posterior dimension, we compared the thickness/myelination ratio of the two deeper sulci (*spls* and *mcgs*) and the two shallow sulci inferior to them (*sspls* and *ifrms*, respectively) with a three-way ANOVA using sulcal type (primary/secondary and tertiary), anatomical position [anterior (*mcgs* and *ifrms*) and posterior (*spls* and *sspls*)], and hemisphere (left and right) as factors.

Predictive labeling of sulcal location using CNNs. For full methodological details, please see Lyu *et al.* (*56*), which describes the methodological pipeline in full. Briefly, the ability to automatically define PMC sulci was compared using two methods: CBA (described in the next paragraph) and deep learning (CNN) with context-aware training. For the CNN, the algorithms were trained on sulcal labels in a fivefold cross-validation manner (60% of participants for training), and then the trained model was chosen with peak performance on the validation set (20% of participants) for each fold. The overall performance was iteratively calculated on the left-out participant in the test set (20% of participants). This approach was developed previously on sulci in LPFC by Lyu *et al.* (*56*) and applied here to PMC sulci. The implementation of the CNN contains two key modifications compared to other CNNs: During the learning phase, surface data augmentation and context-aware training are implemented. The former adds flexibility by implementing intermediate deformations (if needed) to better align sulci across participants and to enhance the model generalizability. The latter incorporates the spatial information of the primary and secondary sulci to guide the automatic labeling of the small and more variable sulci. Prediction performance was determined by calculating the Dice coefficient

between the predicted sulcus and the ground truth, manually defined sulcus using the following formula

$$DICE(X, Y) = \frac{2|X \cap Y|}{|X| + |Y|}$$

Prediction performances for CBA and deep learning with context-aware training were compared using a paired *t* test.

Predictive labeling of sulcal location using CBA. First, all sulcal labels were registered to a common surface template surface (fsaverage) using CBA (*72*). Sulcal probability maps were then calculated to describe the vertices with the highest alignment across participants for a given sulcus. A map was generated for each sulcus by calculating, at each vertex in the fsaverage hemisphere, the number of participants with that vertex labeled as a given sulcus, divided by the total number of participants. The map was then made more precise by constraining the original probability maps into maximum probability maps by only including vertices where (i) more than 33% of participants were included in the given sulcal label and (ii) the sulcus with the highest value of participant overlap was assigned to a given vertex. This step also helped to avoid overlap among sulci. In a leave-one-out cross-validation procedure, probability maps were generated from the combined young adult sample from $N = 71$ participants. These maps were then registered to (i) the held-out participant's native cortical surface, separately for each dataset, and (ii) the held-out participant's native cortical surface of the opposing dataset. Prediction performance was again determined by calculating the Dice coefficient between the predicted sulcus and the manually defined sulcus.

Functional analyses

Creating sulcal connectivity fingerprints from resting-state network parcellations. To determine whether the *ifrms* is functionally distinct from the nearby *spls*, we generated functional connectivity profiles (connectivity fingerprints) using a recently developed analysis (*21*). This analysis implements a four-pronged approach. First, resting-state network parcellations for each individual participant were used from Kong *et al.* (*41*), who generated individual network definitions by applying a hierarchical Bayesian network algorithm to produce maps for each of the 17 networks in individual HCP participants. These data were calculated in the template HCP fs_LR 32k space. This parcellation was conducted blind to both cortical folding and our sulcal definitions. Second, we resampled the network profiles for each participant onto the fsaverage cortical surface and then to each native surface using CBIG tools (https://github.com/ThomasYeoLab/CBIG). Third, we then calculated the overlap between a sulcus with each of the 17 resting-state networks for each participant via the Dice coefficient. Fourth, a three-way (sulcus, network, and hemisphere) rm-ANOVA was run to determine whether the network profiles of the *ifrms* and the more posterior *spls* were differentiable from one another. The functional networks included in the statistical analyses were limited to the DMN and CCN since only these networks overlapped prominently with these sulci. The same analyses, but for the three sulcal *prcus* components, are included in the Supplementary Materials and visualized in fig. S11.

Determining whether the location of the ifrms is predictive of CCN-b and CCN-c. Building off of the functional findings for the *ifrms*, we aimed to quantify whether the location of the *ifrms* was predictive of the location of the two CCN subregions that it overlapped with most (CCN-b and CCN-c), especially the smaller CCN-b. To test this, we leveraged the mean Right, Anterior, Superior (RAS) values of the *ifrms* and the two CCNs obtained in the previous analyses to conduct linear regressions for each hemisphere between the mean RAS coordinates of the *ifrms* (predictor) and CCN-b or CCN-c (outcome).

Determining whether the location of the ifrms is predictive of functional regions from other parcellations in individual participants: MSC. To test that the structure-functional correspondence is not specific to the parcellation from Kong *et al.* (*41*), we generated functional connectivity profiles (connectivity fingerprints) leveraging the data for the 10 subjects from the MSC [5 females and 5 males; ages 24 to 34 years; see (*42*) for additional details on the sample and neuroimaging data]. Briefly, T1s and functional parcellations were collected from the MSC's online repository (https://openfmri.org/dataset/ds000224/). Cortical surface reconstructions were generated with FreeSurfer, and the PMC sulci (192 additional sulci) were defined in all 10 participants by E.H.W. and B.J.P., and confirmed by K.S.W. (see fig. S12). The functional parcellations were resampled from fs_LR 32k space for each participant onto the fsaverage cortical surface, and then to each native surface with Workbench Commands (wb_command). We then used the mri_binarize FreeSurfer function on the six functional networks within the PMC (cingulo-operular, context, frontoparietal, default, parietal memory, and salience) to convert these networks into label files that can be imported and quantified with tools in tksurfer. After defining these networks in each participant, we then calculated the overlap between the *ifrms* and *spls* with each of the six resting-state networks for each participant via the Dice coefficient. Last, a three-way (sulcus, network, and hemisphere) rm-ANOVA was run to once again test whether the network profiles of the *ifrms* and *spls* were differentiable.

Determining whether the ifrms is a functional landmark beyond analyses in individual participants: Meta-analyses. To further investigate the functional relevance of the *ifrms*, maps for search terms (cognitive control, default mode, and frontoparietal network) were created using association tests in Neurosynth (https://neurosynth.org) (*44*) and projected onto the MNI2009b surface. As this surface has a discernible *ifrms* in each hemisphere (see fig. S15A), this process allows us to assess the functional relevance of the *ifrms* across 598, 777, and 116 studies, respectively. We also repeated this process considering a combinatory meta-analysis across association terms suggested by a recent preprint from the OHBM WHATNET [cognitive control, frontoparietal, executive, demand (proxy for multiple demand), and domain general] (*45*).

Examining morphological features of the *ifrms* across the life span and between species

Participants

This part of the study leveraged three human neuroimaging datasets. The first was composed of the combined young adult samples ($N = 72$ participants) described previously. The second human dataset was composed of juveniles, and the third consisted of healthy older adults. For comparative analyses, one chimpanzee neuroimaging dataset was used.

Human (juveniles). Seventy-two participants (30 females and 42 males) were randomly selected from the Neurodevelopment of Reasoning Ability study (*78*). This sample consists of typically developing individuals between the ages of 6 and 18 years (average ± SD = 11.89 ± 3.53). All participants were screened for neurological impairments, psychiatric illness, history of learning disability, and developmental delay. In addition, all participants and their parents gave their informed assent or consent to participate in the study,

which was approved by the Committee for the Protection of Human participants at the University of California, Berkeley.

Human (healthy older adults). Seventy-two healthy older adult participants (37 females and 35 males) with ages ranging from 64 to 90 years old (average ± SD = 74.49 ± 5.15) were randomly selected from the Alzheimer's Disease Neuroimaging Initiative (ADNI) database (adni.loni.usc.edu).

Chimpanzee. Sixty (37 female and 23 male) chimpanzee (*Pan troglodytes*) anatomical T1 scans were chosen from the National Chimpanzee Brain Resource (www.chimpanzee brain.org; supported by NIH grant NS092988). Chimpanzees were between the ages of 9 and 51 years (average ± SD = 23.16 ± 9.75). The chimpanzees were members of the colony housed at the Yerkes National Primate Research Center (YNPRC) of Emory University. All methods were carried out in accordance with YNPRC and Emory University's Institutional Animal Care and Use Committee guidelines. Institutional approval was obtained before the onset of data collection. Further data collection details are described in Keller *et al.* (*79*). These are the same 60 chimpanzee cortical surfaces examined in Miller *et al.* (*53*).

Imaging data acquisition

Human (juveniles). Two high-resolution T1w magnetization-prepared rapid-acquisition gradient echo (MPRAGE) anatomical scans [Repetition Time (TR) = 2300 ms, Echo Time (TE) = 2.98 ms, 1 mm by 1 mm by 1 mm voxels] were acquired using the Siemens 3T Trio fMRI scanner at the University of California, Berkeley Brain Imaging Center.

Human (healthy older adults). T1w MPRAGE anatomical scans were obtained for cortical morphometric analyses in these participants from the ADNI online repository (http://adni.loni.usc.edu). The exact scanning parameters varied across the sample (see table S18 for a breakdown of the different scanning parameters used).

Chimpanzee. Here, we briefly describe the scanning parameters that are described in more thorough detail in Keller *et al.* (*79*). The T1w PRAGE MR images were obtained using the Siemens 3T Trio MR system (TR = 2300 ms, TE = 4.4 ms, TI = 1100 ms, flip angle = 8, field of view = 200 mm by 200 mm) at YNPRC in Atlanta, GA. Before reconstructing the cortical surface, each chimpanzee T1 was scaled to the size of the human brain. As described in Hopkins *et al.* (*80*), within FMRIB Software Library (FSL), (i) the BET function was used to automatically strip away the skull, (ii) the FAST function was used to correct for intensity variations due to magnetic susceptibility artifacts and radio frequency field inhomogeneities (i.e., bias field correction), and (iii) the FLIRT function was used to normalize the isolated brain to the MNI152 template brain using a seven–degree of freedom transformation (i.e., three translations, three rotations, and one uniform scaling), which preserved the shape of individual brains. Afterward, each T1 was segmented using FreeSurfer. The fact that the brains are already isolated, along with bias-field correction and size normalization, greatly assisted in segmenting the chimpanzee brain in FreeSurfer. Furthermore, the initial use of FSL also has the specific benefit of enabling the individual brains to be spatially normalized with preserved brain shape. Last, the values of this transformation matrix and the scaling factor were saved for later use.

Cortical surface reconstruction

Each T1w image was visually inspected for scanner artifacts. Afterward, reconstructions of the cortical surfaces were generated for each participant from their T1 scans using a standard FreeSurfer pipeline [FreeSurfer (v6.0.0): surfer.nmr.mgh.harvard.edu/] (*70*–*72*). Cortical surface reconstructions were created from the resulting boundary made from segmenting the gray and white matter in each anatomical volume with FreeSurfer's automated segmentation tools (*70*). Each reconstruction was inspected for segmentation errors, which were then manually corrected when necessary. As in young adults, all subsequent sulcal labeling and extraction of anatomical metrics were calculated from cortical surface reconstructions from individual participants.

Developmental and comparative analysis of the ifrms

Sulcal labeling. The same 8 to 11 PCC and PRC sulci defined in young adults were manually identified in individual juvenile and healthy older human hemispheres, and the *ifrms* was defined (when present) in chimpanzee hemispheres. Since the *mcgs* and *spls* are present in the PCC of nonhuman hominoids (*63*), as in humans, an indentation was labeled as the *ifrms* if it was (i) inferior to the *mcgs* and (ii) anterior to the *spls*. The specific procedure for sulcal labeling was identical to the methodology described for defining sulci in young adults.

Sulcal depth and cortical thickness. Raw values (in millimeters) for sulcal depth, measured as the distance from the fundus to the smoothed outer pial surface, were calculated with the custom-modified algorithm used in the previous section (*75*). These depth values were then normalized to the maximal depth within each individual hemisphere, which is located within the insula for both species (*53*). Mean cortical thickness values (in millimeters) for each sulcus were calculated with the mris_anatomical_stats FreeSurfer function and also normalized to the thickest vertex within each individual hemisphere (*76*). Similar to previous work (*53*), we also demonstrate that the observed sulcal morphological patterns hold regardless of whether raw (fig. S20) or normalized values are used (Fig. 7, C and D). Like in young adults, the depth (in millimeters), mean cortical thickness values (in millimeters), and mean surface area (in square millimeters) were also extracted from all juvenile and healthy older adult human PMC sulci.

Quantitatively assessing the developmental and comparative differences of the ifrms morphology. A three-way ANOVA with factors hemisphere (left and right), age group (juvenile, young adult, and older), and species (human and chimpanzee) was run for each morphological feature. To address age differences in the chimpanzee dataset, the chimpanzees who had an *ifrms* were divided into similar age ranges reflecting the respective ranges across the human datasets: juvenile chimpanzees (age <22), young adult chimpanzees ($22 \leq$ age ≤ 36), and older chimpanzees (age >36). Three chimpanzees did not have ages provided and were therefore excluded from the morphological analyses.

Identifying the ifrms in postmortem hominoid and nonhuman primate brains

To determine whether the *ifrms* is present in nonhuman primates and nonhuman hominoids, beyond the in vivo chimpanzee participants, we identified indentations in the cerebral cortex (when present) inferior to the *mcgs* and anterior to the *spls*, within images of Old World monkey, New World monkey, and nonhuman hominoid (chimpanzees, gorillas, and orangutans) postmortem hemispheres from a classic atlas by Gustaf (*81*).

Quantitatively classifying the ifrms on the basis of morphology

We used k-means clustering on the primary descriptive features of tertiary sulci (depth and surface area; Fig. 2 and fig. S22) to classify the *ifrms* (human: left = 216, right = 216; chimpanzee: left = 28, right = 27; total across species: left = 244, right = 243). The optimal number of clusters was quantitatively determined using the NbClust function from the NbClust R package, which leverages 30 indices to propose the best number of clusters for the data (based on the majority rule). The NbClust function and k-means clustering algorithm were

run on scaled *ifrms* morphological data—separately in each hemisphere. Cluster plots were generated using the ggscatter function from the ggpubr R package to visualize the results.

Statistical methods

All statistical tests were implemented in R (v4.0.1) and RStudio (v1.3.959). Chi-squared tests were carried out with the chisq.test function, and post hoc pairwise comparisons were run with the chisq.multcomp function from the built-in R stats and RVAideMemoire R packages, respectively. All ANOVAs (regular and rm) were implemented using the aov function from the built-in R stats package. Post hoc *t* tests were conducted for the significant ANOVA effects and implemented with the emmeans R package. Effect sizes for the ANOVA effects are reported with the generalized eta-squared (η^2G) metric and computed with the anova_summary function from the rstatix R package. K-means clustering was implemented using the kmeans function from the built-in R stats package. The paired *t* test was carried out with the t.test function from the built-in R stats package. The effect size of this *t* test is reported with the Cohen's d (*d*) metric and obtained with the cohens_d function from the rstatix R package. Linear regression analyses were run using the lm function from the built-in R stats package.

SUPPLEMENTARY MATERIALS

Supplementary material for this article is available at https://science.org/doi/10.1126/sciadv.abn9516

View/request a protocol for this paper from *Bio-protocol*.

REFERENCES AND NOTES

1. P. Rakic, Specification of cerebral cortical areas. *Science* **241**, 170–176 (1988).
2. W. Welker, in *Cerebral Cortex: Comparative Structure and Evolution of Cerebral Cortex, Part II*, E. G. Jones, A. Peters, Eds. (Springer US, 1990), pp. 3–136.
3. K. Zilles, N. Palomero-Gallagher, K. Amunts, Development of cortical folding during evolution and ontogeny. *Trends Neurosci.* **36**, 275–284 (2013).
4. D. C. Van Essen, C. J. Donahue, M. F. Glasser, Development and evolution of cerebral and cerebellar cortex. *Brain Behav. Evol.* **91**, 158–169 (2018).
5. K. Zilles, E. Armstrong, A. Schleicher, H.-J. Kretschmann, The human pattern of gyrification in the cerebral cortex. *Anat. Embryol.* **179**, 173–179 (1988).
6. D. C. Van Essen, in *Evolution of Nervous Systems*, J. H. Kaas, Ed. (Academic Press, 2007), pp. 267–276.
7. D. J. Cunningham, *Contribution to the Surface Anatomy of the Cerebral Hemispheres* (Academy House, 1892).
8. G. E. Smith, A new topographical survey of the human cerebral cortex, being an account of the distribution of the anatomically distinct cortical areas and their relationship to the cerebral sulci. *J. Anat. Physiol.* **41**, 237–254 (1907).
9. B. A. Wandell, J. Winawer, Imaging retinotopic maps in the human brain. *Vision Res.* **51**, 718–737 (2011).
10. N. C. Benson, O. H. Butt, R. Datta, P. D. Radoeva, D. H. Brainard, G. K. Aguirre, The retinotopic organization of striate cortex is well predicted by surface topology. *Curr. Biol.* **22**, 2081–2085 (2012).
11. K. S. Weiner, G. Golarai, J. Caspers, M. R. Chuapoco, H. Mohlberg, K. Zilles, K. Amunts, K. Grill-Spector, The mid-fusiform sulcus: A landmark identifying both cytoarchitectonic and functional divisions of human ventral temporal cortex. *Neuroimage* **84**, 453–465 (2014).
12. K. S. Weiner, K. Zilles, The anatomical and functional specialization of the fusiform gyrus. *Neuropsychologia* **83**, 48–62 (2016).
13. K. S. Weiner, The mid-fusiform sulcus (*sulcus sagittalis gyri fusiformis*). *Anat. Rec.* **302**, 1491–1503 (2019).
14. G. C. Ribas, A. Yasuda, E. C. Ribas, K. Nishikuni, A. J. Rodrigues Jr., Surgical anatomy of microneurosurgical sulcal key points. *Oper. Neurosurg.* **59**, ONS177-210 (2006).
15. A. Fornito, M. Yücel, S. Wood, G. W. Stuart, J.-A. Buchanan, T. Proffitt, V. Anderson, D. Velakoulis, C. Pantelis, Individual differences in anterior cingulate/paracingulate morphology are related to executive functions in healthy males. *Cereb. Cortex* **14**, 424–431 (2004).
16. A. Fornito, M. Yücel, S. J. Wood, T. Proffitt, P. D. McGorry, D. Velakoulis, C. Pantelis, Morphology of the paracingulate sulcus and executive cognition in schizophrenia. *Schizophr. Res.* **88**, 192–197 (2006).
17. G. Borst, A. Cachia, J. Vidal, G. Simon, C. Fischer, A. Pineau, N. Poirel, J.-F. Mangin, O. Houdé, Folding of the anterior cingulate cortex partially explains inhibitory control during childhood: A longitudinal study. *Dev. Cogn. Neurosci.* **9**, 126–135 (2014).
18. J. R. Garrison, C. Fernyhough, S. McCarthy-Jones, M. Haggard; Australian Schizophrenia Research Bank, J. S. Simons, Paracingulate sulcus morphology is associated with hallucinations in the human brain. *Nat. Commun.* **6**, 8956 (2015).
19. C. Amiez, C. R. E. Wilson, E. Procyk, Variations of cingulate sulcal organization and link with cognitive performance. *Sci. Rep.* **8**, 1–13 (2018).
20. A. Lopez-Persem, L. Verhagen, C. Amiez, M. Petrides, J. Sallet, The human ventromedial prefrontal cortex: Sulcal morphology and its influence on functional organization. *J. Neurosci.* **39**, 3627–3639 (2019).
21. J. A. Miller, W. I. Voorhies, D. J. Lurie, M. D'Esposito, K. S. Weiner, Overlooked tertiary sulci serve as a meso-scale link between microstructural and functional properties of human lateral prefrontal cortex. *J. Neurosci.* **41**, 2229–2244 (2021).
22. W. I. Voorhies, J. A. Miller, J. K. Yao, S. A. Bunge, K. S. Weiner, Cognitive insights from tertiary sulci in prefrontal cortex. *Nat. Commun.* **12**, 5122 (2021).
23. F. Sanides, Structure and function of the human frontal lobe. *Neuropsychologia* **2**, 209–219 (1964).
24. M. E. Raichle, A. M. MacLeod, A. Z. Snyder, W. J. Powers, D. A. Gusnard, G. L. Shulman, A default mode of brain function. *Proc. Natl. Acad. Sci. U.S.A.* **98**, 676–682 (2001).
25. R. L. Buckner, J. R. Andrews-Hanna, D. L. Schacter, The brain's default network: Anatomy, function, and relevance to disease. *Ann. N. Y. Acad. Sci.* **1124**, 1–38 (2008).
26. R. Leech, J. Smallwood, The posterior cingulate cortex: Insights from structure and function. *Cingulate Cortex* **166**, 73–85 (2019).
27. J. Smallwood, B. C. Bernhardt, R. Leech, D. Bzdok, E. Jefferies, D. S. Margulies, The default mode network in cognition: A topographical perspective. *Nat. Rev. Neurosci.* **22**, 503–513 (2021).
28. D. L. Schacter, D. R. Addis, R. L. Buckner, Remembering the past to imagine the future: The prospective brain. *Nat. Rev. Neurosci.* **8**, 657–661 (2007).
29. P. Hagmann, L. Cammoun, X. Gigandet, R. Meuli, C. J. Honey, V. J. Wedeen, O. Sporns, Mapping the structural core of human cerebral cortex. *PLOS Biol.* **6**, e159 (2008).
30. D. S. Margulies, J. L. Vincent, C. Kelly, G. Lohmann, L. Q. Uddin, B. B. Biswal, A. Villringer, F. Xavier Castellanos, M. P. Milham, M. Petrides, Precuneus shares intrinsic functional architecture in humans and monkeys. *Proc. Natl. Acad. Sci. U.S.A.* **106**, 20069–20074 (2009).
31. J. M. Pearson, S. R. Heilbronner, D. L. Barack, B. Y. Hayden, M. L. Platt, Posterior cingulate cortex: Adapting behavior to a changing world. *Trends Cogn. Sci.* **15**, 143–151 (2011).
32. R. Leech, D. J. Sharp, The role of the posterior cingulate cortex in cognition and disease. *Brain* **137**, 12–32 (2014).
33. H. Grydeland, L. T. Westlye, K. B. Walhovd, A. M. Fjell, Intracortical posterior cingulate myelin content relates to error processing: Results from T1- and T2-weighted MRI myelin mapping and electrophysiology in healthy adults. *Cereb. Cortex* **26**, 2402–2410 (2016).
34. J. Parvizi, G. W. Van Hoesen, J. Buckwalter, A. Damasio, Neural connections of the posteromedial cortex in the macaque. *Proc. Natl. Acad. Sci. U.S.A.* **103**, 1563–1568 (2006).
35. D. S. Margulies, S. S. Ghosh, A. Goulas, M. Falkiewicz, J. M. Huntenburg, G. Langs, G. Bezgin, S. B. Eickhoff, F. X. Castellanos, M. Petrides, E. Jefferies, J. Smallwood, Situating the default-mode network along a principal gradient of macroscale cortical organization. *Proc. Natl. Acad. Sci. U.S.A.* **113**, 12574–12579 (2016).
36. T. Xu, K.-H. Nenning, E. Schwartz, S.-J. Hong, J. T. Vogelstein, A. Goulas, D. A. Fair, C. E. Schroeder, D. S. Margulies, J. Smallwood, M. P. Milham, G. Langs, Cross-species functional alignment reveals evolutionary hierarchy within the connectome. *Neuroimage* **223**, 117346 (2020).
37. V. J. Sydnor, B. Larsen, D. S. Bassett, A. Alexander-Bloch, D. A. Fair, C. Liston, A. P. Mackey, M. P. Milham, A. Pines, D. R. Roalf, J. Seidlitz, T. Xu, A. Raznahan, T. D. Satterthwaite, Neurodevelopment of the association cortices: Patterns, mechanisms, and implications for psychopathology. *Neuron* **109**, 2820–2846 (2021).
38. R. L. Buckner, L. M. DiNicola, The brain's default network: Updated anatomy, physiology and evolving insights. *Nat. Rev. Neurosci.* **20**, 593–608 (2019).
39. J. A. Miller, M. D'Esposito, K. S. Weiner, Using tertiary sulci to map the "cognitive globe" of prefrontal cortex. *J. Cogn. Neurosci.* 1–18 (2021).
40. M. Petrides, *Atlas of the Morphology of the Human Cerebral Cortex on the Average MNI Brain* (Academic Press, 2019).
41. R. Kong, J. Li, C. Orban, M. R. Sabuncu, H. Liu, A. Schaefer, N. Sun, X.-N. Zuo, A. J. Holmes, S. B. Eickhoff, B. T. T. Yeo, Spatial topography of individual-specific cortical networks predicts human cognition, personality, and emotion. *Cereb. Cortex* **29**, 2533–2551 (2019).
42. E. M. Gordon, T. O. Laumann, A. W. Gilmore, D. J. Newbold, D. J. Greene, J. J. Berg, M. Ortega, C. Hoyt-Drazen, C. Gratton, H. Sun, J. M. Hampton, R. S. Coalson, A. L. Nguyen, K. B. McDermott, J. S. Shimony, A. Z. Snyder, B. L. Schlaggar, S. E. Petersen, S. M. Nelson, N. U. F. Dosenbach, Precision functional mapping of individual human brains. *Neuron* **95**, 791–807.e7 (2017).

43. M. F. Glasser, T. S. Coalson, E. C. Robinson, C. D. Hacker, J. Harwell, E. Yacoub, K. Ugurbil, J. Andersson, C. F. Beckmann, M. Jenkinson, S. M. Smith, D. C. Van Essen, A multi-modal parcellation of human cerebral cortex. *Nature* **536**, 171–178 (2016).
44. T. Yarkoni, R. A. Poldrack, T. E. Nichols, D. C. Van Essen, T. D. Wager, Large-scale automated synthesis of human functional neuroimaging data. *Nat. Methods* **8**, 665–670 (2011).
45. L. Q. Uddin, R. F. Betzel, J. R. Cohen, J. S. Damoiseaux, F. De Brigard, S. Eickhoff, A. Fornito, C. Gratton, E. M. Gordon, A. Laird, L. J. Larson-Prior, A. R. McIntosh, L. D. Nickerson, L. P. Ana L. Pinho, R. Poldrack, A. Razi, S. Sadaghiani, J. M. Shine, A. Yendiki, B. T. Thomas Yeo, R. N. Spreng, Controversies and current progress on large-scale brain network nomenclature from OHBM WHATNET: Workgroup for HArmonized Taxonomy of NETworks (2022).
46. M. Ono, S. Kubik, C. D. Abernathey, *Atlas of the Cerebral Sulci* (G. Thieme Verlag, 1990).
47. L. Borne, D. Rivière, M. Mancip, J.-F. Mangin, Automatic labeling of cortical sulci using patch- or CNN-based segmentation techniques combined with bottom-up geometric constraints. *Med. Image Anal.* **62**, 101651 (2020).
48. K. Drudik, V. Zlatkina, M. Petrides, Morphological patterns and spatial probability maps of the superior parietal sulcus in the human brain. *Cereb. Cortex* , bhac132 (2022).
49. G. Retzius, *Das Menschenhirn: Studien in der makroskopischen Morphologie* (Königliche Buchdruckerei P. A. Norstedt & Söner, 1896).
50. J. Gomez, Z. Zhen, K. S. Weiner, Human visual cortex is organized along two genetically opposed hierarchical gradients with unique developmental and evolutionary origins. *PLOS Biol.* **17**, e3000362 (2019).
51. X. Chen, X. Liu, B. J. Parker, Z. Zhen, K. S. Weiner, Functionally and structurally distinct fusiform face area(s) in over 1000 participants. bioRxiv 2022.04.08.487562 (2022).
52. V. S. Natu, J. Gomez, M. Barnett, B. Jeska, E. Kirilina, C. Jaeger, Z. Zhen, S. Cox, K. S. Weiner, N. Weiskopf, K. Grill-Spector, Apparent thinning of human visual cortex during childhood is associated with myelination. *Proc. Natl. Acad. Sci. U.S.A.* **116**, 20750–20759 (2019).
53. J. A. Miller, W. I. Voorhies, X. Li, I. Raghuram, N. Palomero-Gallagher, K. Zilles, C. C. Sherwood, W. D. Hopkins, K. S. Weiner, Sulcal morphology of ventral temporal cortex is shared between humans and other hominoids. *Sci. Rep.* **10**, 17132 (2020).
54. C. Amiez, J. Sallet, W. D. Hopkins, A. Meguerditchian, F. Hadj-Bouziane, S. Ben Hamed, C. R. E. Wilson, E. Procyk, M. Petrides, Sulcal organization in the medial frontal cortex provides insights into primate brain evolution. *Nat. Commun.* **10**, 3437 (2019).
55. M. Yucel, G. W. Stuart, P. Maruff, D. Velakoulis, S. F. Crowe, G. Savage, C. Pantelis, Hemispheric and gender-related differences in the gross morphology of the anterior cingulate/paracingulate cortex in normal volunteers: An MRI morphometric study. *Cerebral. Cortex* **11**, 17–25 (2001).
56. I. Lyu, S. Bao, L. Hao, J. Yao, J. A. Miller, W. Voorhies, W. D. Taylor, S. A. Bunge, K. S. Weiner, B. A. Landman, Labeling lateral prefrontal sulci using spherical data augmentation and context-aware training. *Neuroimage* **229**, 117758 (2021).
57. B. A. Vogt, L. Vogt, S. Laureys, Cytology and functionally correlated circuits of human posterior cingulate areas. *Neuroimage* **29**, 452–466 (2006).
58. B. A. Vogt, N. Palomero-Gallagher, in *The Human Nervous System (Third Edition)*, J. K. Mai, G. Paxinos, Eds. (Academic Press, 2012), pp. 943–987.
59. K. Amunts, H. Mohlberg, S. Bludau, K. Zilles, Julich-Brain: A 3D probabilistic atlas of the human brain's cytoarchitecture. *Science* **369**, 988–992 (2020).
60. E. M. Gordon, C. J. Lynch, C. Gratton, T. O. Laumann, A. W. Gilmore, D. J. Greene, M. Ortega, A. L. Nguyen, B. L. Schlaggar, S. E. Petersen, N. U. F. Dosenbach, S. M. Nelson, Three distinct sets of connector hubs integrate human brain function. *Cell Rep.* **24**, 1687–1695.e4 (2018).
61. B. Y. Hayden, A. C. Nair, A. N. McCoy, M. L. Platt, Posterior cingulate cortex mediates outcome-contingent allocation of behavior. *Neuron* **60**, 19–25 (2008).
62. B. Y. Hayden, D. V. Smith, M. L. Platt, Electrophysiological correlates of default-mode processing in macaque posterior cingulate cortex. *Proc. Natl. Acad. Sci U.S.A.* **106**, 5948–5953 (2009).
63. B. A. Vogt, L. Vogt, N. B. Farber, G. Bush, Architecture and neurocytology of monkey cingulate gyrus. *J. Comp. Neurol.* **485**, 218–239 (2005).
64. E. Armstrong, A. Schleicher, H. Omran, M. Curtis, K. Zilles, The ontogeny of human gyrification. *Cereb. Cortex.* **5**, 56–63 (1995).
65. J. G. Chi, E. C. Dooling, F. H. Gilles, Gyral development of the human brain. *Ann. Neurol.* **1**, 86–93 (1977).
66. L. Brun, G. Auzias, M. Viellard, N. Villeneuve, N. Girard, F. Poinso, D. Da Fonseca, C. Deruelle, Localized misfolding within Broca's area as a distinctive feature of autistic disorder. *Biol. Psychiatry Cogn. Neurosci. Neuroimaging* **1**, 160–168 (2016).
67. C. J. Ammons, M.-E. Winslett, J. Bice, P. Patel, K. E. May, R. K. Kana, The mid-fusiform sulcus in autism spectrum disorder: Establishing a novel anatomical landmark related to face processing. *Autism Res.* **14**, 53–64 (2021).
68. C. J. Lynch, L. Q. Uddin, K. Supekar, A. Khouzam, J. Phillips, V. Menon, Default mode network in childhood autism: Posteromedial cortex heterogeneity and relationship with social deficits. *Biol. Psychiatry* **74**, 212–219 (2013).
69. D. C. Van Essen, K. Ugurbil, E. Auerbach, D. Barch, T. E. J. Behrens, R. Bucholz, A. Chang, L. Chen, M. Corbetta, S. W. Curtiss, S. D. Penna, D. Feinberg, M. F. Glasser, N. Harel, A. C. Heath, L. Larson-Prior, D. Marcus, G. Michalareas, S. Moeller, R. Oostenveld, S. E. Petersen, F. Prior, B. L. Schlaggar, S. M. Smith, A. Z. Snyder, J. Xu, E. Yacoub; WU-Minn HCP Consortium, The human connectome project: A data acquisition perspective. *Neuroimage* **62**, 2222–2231 (2012).
70. A. M. Dale, B. Fischl, M. I. Sereno, Cortical surface-based analysis. I. Segmentation and surface reconstruction. *Neuroimage* **9**, 179–194 (1999).
71. B. Fischl, M. I. Sereno, A. M. Dale, Cortical surface-based analysis. II: Inflation, flattening, and a surface-based coordinate system. *Neuroimage* **9**, 195–207 (1999).
72. B. Fischl, M. I. Sereno, R. B. Tootell, A. M. Dale, High-resolution intersubject averaging and a coordinate system for the cortical surface. *Hum. Brain Mapp.* **8**, 272–284 (1999).
73. M. F. Glasser, S. N. Sotiropoulos, J. A. Wilson, T. S. Coalson, B. Fischl, J. L. Andersson, J. Xu, S. Jbabdi, M. Webster, J. R. Polimeni, D. C. Van Essen, M. Jenkinson; WU-Minn HCP Consortium, The minimal preprocessing pipelines for the human connectome project. *Neuroimage* **80**, 105–124 (2013).
74. B. A. Vogt, E. A. Nimchinsky, L. J. Vogt, P. R. Hof, Human cingulate cortex: Surface features, flat maps, and cytoarchitecture. *J. Comp. Neurol.* **359**, 490–506 (1995).
75. C. R. Madan, Robust estimation of sulcal morphology. *Brain Inform.* **6**, 5 (2019).
76. B. Fischl, A. M. Dale, Measuring the thickness of the human cerebral cortex from magnetic resonance images. *Proc. Natl. Acad. Sci. U.S.A.* **97**, 11050–11055 (2000).
77. M. F. Glasser, D. C. Van Essen, Mapping human cortical areas in vivo based on myelin content as revealed by T1- and T2-weighted MRI. *J. Neurosci.* **31**, 11597–11616 (2011).
78. E. Ferrer, K. J. Whitaker, J. S. Steele, C. T. Green, C. Wendelken, S. A. Bunge, White matter maturation supports the development of reasoning ability through its influence on processing speed. *Dev. Sci.* **16**, 941–951 (2013).
79. S. S. Keller, N. Roberts, W. Hopkins, A comparative magnetic resonance imaging study of the anatomy, variability, and asymmetry of Broca's area in the human and chimpanzee brain. *J. Neurosci.* **29**, 14607–14616 (2009).
80. W. D. Hopkins, X. Li, T. Crow, N. Roberts, Vertex- and atlas-based comparisons in measures of cortical thickness, gyrification and white matter volume between humans and chimpanzees. *Brain Struct. Funct.* **222**, 229–245 (2017).
81. R. Gustaf, *Cerebra simiarum illustrata. Das Affenhirn in bildlicher Darstellung* (Stockholm,Centraldruckerei, 1906).
82. E. M. Gordon, T. O. Laumann, B. Adeyemo, A. W. Gilmore, S. M. Nelson, N. U. F. Dosenbach, S. E. Petersen, Individual-specific features of brain systems identified with resting state functional correlations. *Neuroimage* **146**, 918–939 (2017).
83. A. Ecker. *Die Hirnwindungen des Menschen* (F. Vieweg u. Sohn, 1869).
84. E. Huschke, *Schaedel, Hirn und Seele des Menschen und der Thiere nach Alter, Geschlecht und Race: dargestellt nach neuen Methoden und Untersuchungen* (Mauke, 1854).
85. A. Ecker, *On the Convolutions of the Human Brain* (Smith, Elder & Company, 1873).
86. H. J. ten Donkelaar, D. Kachlík, R. Shane Tubbs, *An Illustrated Terminologia Neuroanatomica: A Concise Encyclopedia of Human Neuroanatomy* (Springer, 2018).
87. H. J. T. ten Donkelaar, H. J. ten Donkelaar, N. Tzourio-Mazoyer, J. K. Mai, Toward a common terminology for the gyri and sulci of the human cerebral cortex. *Front. Neuroanat.* **12**, 93 (2018).
88. E. A. Spitzka, The post-mortem examination of Leon F. Czolgosz, the assassin of President McKinley. *Am. J. Psychiatry* **58**, 386–404 (1902).
89. E. A. Spitzka, A study of the brains of six eminent scientists and scholars belonging to the American Anthropometric Society, together with a description of the skull of Professor E. D. Cope. *Trans. Am. Philos. Soc.* **21**, 175 (1907).
90. S. F. Witelson, D. L. Kigar, T. Harvey, The exceptional brain of Albert Einstein. *Lancet* **353**, 2149–2153 (1999).
91. D. Falk, F. E. Lepore, A. Noe, The cerebral cortex of Albert Einstein: A description and preliminary analysis of unpublished photographs. *Brain* **136**, 1304–1327 (2013).
92. K. S. Weiner, On (ab)normality: Einstein's fusiform gyrus. *Brain Cogn.* **94**, 1–3 (2015).
93. W. Men, D. Falk, T. Sun, W. Chen, J. Li, D. Yin, L. Zang, M. Fan, The corpus callosum of Albert Einstein's brain: Another clue to his high intelligence? *Brain* **137**, e268 (2014).
94. D. Falk, New information about Albert Einstein's brain. *Front. Evol. Neurosci.* **1**, 3 (2009).
95. D. Falk, Evolution of brain and culture: The neurological and cognitive journey from Australopithecus to Albert Einstein. *J. Anthropol. Sci.* **94**, 99–111 (2016).
96. A. M. Galaburda, Albert Einstein's brain. *Lancet* **354**, 1821–1822 (1999).
97. T. Hines, Neuromythology of Einstein's brain. *Brain Cogn.* **88**, 21–25 (2014).
98. A. W. Campbell, E. B. Schlesinger, H. A. Riley, *Histological Studies on the Localisation of Cerebral Function* (Cambridge Univ. Press, 1905).
99. H. Gray, *Anatomy of the Human Body* (Lea & Febiger, 1878).
100. C. Vogt, O. Vogt, *Allgemeine Ergebnisse unserer Hirnforschung* (J. A. Barth, 1919).
101. C. F. von Economo, G. N. Koskinas, *Die cytoarchitektonik der hirnrinde deserwachsenen menschen* (J. Springer, 1925).
102. P. Bailey, G. von Bonin, *The Isocortex of Man* (University of Illinois Press, 1951).

103. B. A. Vogt, Structural organization of cingulate cortex: Areas, neurons, and somatodendritic transmitter receptors, in *Neurobiology of Cingulate Cortex and Limbic Thalamus*, B. A. Vogt, M. Gabriel, Eds. (Birkhauser, 1993), pp. 19–70.
104. B. A. Vogt, Ed., *Cingulate Neurobiology and Disease* (OUP, 2009).

Acknowledgments: We thank B. Landman for comments and feedback on the deep learning analyses. **Funding:** This research was supported by a T32 HWNI training grant and an NSF-GRFP fellowship (W.I.V.), start-up funds from UC Berkeley (K.S.W.), and NIH R01MH116914 (B.L.F.). Funding for some of the original data collection and curation was provided by NINDS R01 NS057156 (S.A.B.) and NSF BCS1558585 (S.A.B.). Data analysis was supported by NICHD R21HD100858 (K.S.W. and S.A.B.) and NSF CAREER 2042251 (K.S.W.). Alzheimer's Disease Neuroimaging Initiative: Data collection and sharing for this project was funded by the Alzheimer's Disease Neuroimaging Initiative (ADNI) (National Institutes of Health Grant U01 AG024904) and DOD ADNI (Department of Defense award number W81XWH-12-2-0012). ADNI is funded by the National Institute on Aging, the National Institute of Biomedical Imaging and Bioengineering, and through contributions from the following: AbbVie, Alzheimer's Association; Alzheimer's Drug Discovery Foundation; Araclon Biotech; BioClinica Inc.; Biogen; Bristol-Myers Squibb Company; CereSpir Inc.; Cogstate; Eisai Inc.; Elan Pharmaceuticals Inc.; Eli Lilly and Company; EuroImmun; F. Hoffmann-La Roche Ltd. and its affiliated company Genentech Inc.; Fujirebio; GE Healthcare; IXICO Ltd.; Janssen Alzheimer Immunotherapy Research & Development LLC.; Johnson & Johnson Pharmaceutical Research & Development LLC.; Lumosity; Lundbeck; Merck & Co Inc.; Meso Scale Diagnostics LLC.; NeuroRx Research; Neurotrack Technologies; Novartis Pharmaceuticals Corporation; Pfizer Inc.; Piramal Imaging; Servier; Takeda Pharmaceutical Company; and Transition Therapeutics. The Canadian Institutes of Health Research is providing funds to support ADNI clinical sites in Canada. Private sector contributions are facilitated by the Foundation for the National Institutes of Health (www.fnih.org). The grantee organization is the Northern California Institute for Research and Education, and the study is coordinated by the Alzheimer's Therapeutic Research Institute at the University of Southern California. ADNI data are disseminated by the Laboratory for Neuro Imaging at the University of Southern California. Data from young adults were provided by the Human Connectome Project, WU-Minn Consortium (principal investigators: D. Van Essen and K. Ugurbil; 1U54MH091657) funded by the 16 NIH Institutes and Centers that support the NIH Blueprint for Neuroscience Research; and by the McDonnell Center for Systems Neuroscience at Washington University. Data from chimpanzees were provided by the National Chimpanzee Brain Resource (supported by NIH grant NS092988). **Author contributions:** E.H.W., B.J.P., S.A.B., B.L.F., and K.S.W. designed research; E.H.W., B.J.P., W.I.V., J.A.M., I.L., T.H., L.A.-G., S.R.K., and K.S.W. performed research; E.H.W., B.J.P., W.I.V., J.A.M., I.L., T.H., L.A.-G., and S.R.K. analyzed data; E.H.W., B.J.P., S.A.B., B.L.F., and K.S.W. wrote the paper. All authors edited the paper and gave final approval before submission. **Competing interests:** The authors declare that they have no competing interests. **Data and materials availability:** All data needed to evaluate the conclusions in the paper are present in the paper and/or the Supplementary Materials. In addition, all data and code used for this project have been made freely available under the accession code: https://doi.org/10.5281/zenodo.5644409. These data and code are also available on GitHub (as an additional repository; see: https://github.com/cnl-berkeley/stable_projects/tree/main/TripartiteLandmark_PosteriorCingulate). The processed data required to perform all statistical analyses and to reproduce all figures are freely available at either of the above links. Visualizations of all sulcal definitions generated for each participant are provided in the Supplementary Materials. Requests for further information or raw data should be directed to the corresponding author, K.S.W. (kweiner@berkeley.edu).

Submitted 10 January 2022
Accepted 21 July 2022
Published 7 September 2022
10.1126/sciadv.abn9516

Uncovering a tripartite landmark in posterior cingulate cortex

Ethan H. WillbrandBenjamin J. ParkerWilla I. VoorhiesJacob A. MillerIlwoo LyuTyler HallockLyndsey Aponik-GremillionSeth R. KoslovSilvia A. BungeBrett L. FosterKevin S. Weiner

Sci. Adv., 8 (36), eabn9516. • DOI: 10.1126/sciadv.abn9516